Dramatic Impact of Materials Combinations on the Chemical Organization of Core–Shell Nanocrystals: Boosting the Tm^{3+} Emission above 1600 nm

Fernando Arteaga Cardona, Eduard Madirov, Radian Popescu, Di Wang, Dmitry Busko, Dominique Ectors, Christian Kübel, Yolita M. Eggeler, Bernardo A. Arús, Andriy Chmyrov, Oliver T. Bruns, Bryce S. Richards,* and Damien Hudry*

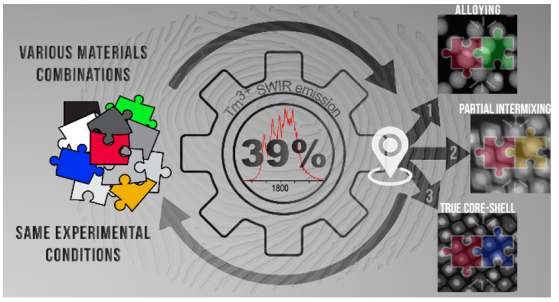

ABSTRACT: This article represents the first foray into investigating the consequences of various material combinations on the short-wave infrared (SWIR, 1000–2000 nm) performance of Tm-based core–shell nanocrystals (NCs) above 1600 nm. In total, six different material combinations involving two different types of SWIR-emitting core NCs (α-$NaTmF_4$ and $LiTmF_4$) combined with three different protecting shell materials (α-$NaYF_4$, CaF_2, and $LiYF_4$) have been synthesized. All corresponding homo- and heterostructured NCs have been meticulously characterized by powder X-ray diffraction and electron microscopy techniques. The latter revealed that out of the six investigated combinations, only one led to the formation of a true core–shell structure with well-segregated core and shell domains. The direct correlation between the downshifting performance and the spatial localization of Tm^{3+} ions within the final homo- and heterostructured NCs is established. Interestingly, to achieve the best SWIR performance, the formation of an abrupt interface is not a prerequisite, while the existence of a pure (even thin) protective shell is vital. Remarkably, although all homo- and heterostructured NCs have been synthesized under the exact same experimental conditions, Tm^{3+} SWIR emission is either fully quenched or highly efficient depending on the type of material combination. The most efficient combination ($LiTmF_4/LiYF_4$) achieved a high photoluminescence quantum yield of 39% for SWIR emission above 1600 nm (excitation power density in the range 0.5–3 W/cm^2) despite significant intermixing. From now on, highly efficient SWIR-emitting probes with an emission above 1600 nm are within reach to unlock the full potential of *in vivo* SWIR imaging.

KEYWORDS: *nanocrystals, core–shell, thulium, material combinations, shortwave infrared, SWIR imaging, photoluminescence quantum yield*

Rare earth (RE)-based core–shell nanocrystals (NCs) constitute an important class of luminescent nanomaterials that were first reported over two decades ago.[1,2] The unique photoluminescent properties associated with these materials (upconversion, downconversion, downshifting) quickly aroused the interest of the scientific community due to the wide variety of potential technological applications that could benefit from the utilization of RE-based core–shell NCs.[3−5] Among these, shortwave infrared (SWIR, 1000–2000 nm) imaging has been attracting growing interest over the past decade[6−8] due to important benefits afforded by RE-based core–shell NCs compared to carbon nanotubes,[9−11] quantum dots,[12−14] or organic dyes.[15,16] For instance, the ability to perform *in vivo* optical imaging in the far end of the SWIR region (i.e., >1600 nm) with a nontoxic host material constitutes a real advantage. Nevertheless, such an advantage is still poorly investigated due to the lack of materials efficiently emitting in that particular region of the SWIR spec-

trum.[13,17−20] Consequently, the real interest and benefit of RE-based core−shell NCs over other SWIR-emitting probes are still difficult to assess (i.e., via a true side-by-side comparison) due to the weak absorption cross-section of RE ions combined with a still-limited downshifting photoluminescent quantum yield (PLQY) in the near-infrared (NIR, 700−1000 nm) to SWIR range. Although the absorption cross-section is an intrinsic characteristic of RE ions and thus hard to modify, the PLQY can be significantly optimized with careful material design.

In the past, various strategies have been explored to boost the PLQY of RE-based NCs and, thus, counterbalance the negative impact of their weak absorption cross-section.[21,22] Among those strategies, the epitaxial growth of an optically inert shell has been a proven efficient strategy to maximize the PLQY.[23] Additionally, in the case of *in vivo* applications, the epitaxial growth strategy also offers a significant advantage regarding the simplicity of the architecture and chemical composition of the SWIR-emitting material. Although, at first sight, the inert shell strategy appears to be very simple, its experimental implementation is less than straightforward. Indeed, over the past few years, conclusive experimental evidence has highlighted the detrimental effect of cation intermixing on the PLQY of RE-based NCs, both for NIR → visible upconversion as well as NIR → SWIR downshifting.[24−27]

Cation intermixing is a complex phenomenon whose underlying mechanisms are still poorly understood. As cation intermixing partially or totally destroys the chemical integrity and spatial confinement of the initially designed core and shell domains, the optical characteristics − such as the emission spectrum and PLQY − can be dramatically affected. The recently recognized importance of cation intermixing has led to a better understanding of the phenomenon[28−30] along with suggested strategies to prevent, or at least mitigating, its detrimental effects on the optical properties.[24,26,31,32]

Since the emergence of RE-based core−shell NCs, homogeneous material combinations have been widely investigated. Indeed, the archetype combination between at least two $NaREF_4$ domains represents, to date, the vast majority of all reported RE-based core−shell NCs. In contrast, investigations dealing with heterogeneous material combinations (i.e., different crystal structures and/or chemical modifications) are still very sparse.[25,33−43] Moreover, the reported heterogeneous material combinations often suffer from a lack of in-depth structural characterization that unambiguously prove the true organization of the synthesized heterostructure.[34,38−43] The utilization of CaF_2 (space group $Fm\bar{3}m$) as the shell domain has been the first heterogeneous combination reported with α-$NaYF_4$:Yb:Er (space group $Fm\bar{3}m$) to improve upconversion emission beyond that achieved by its homogeneous counterpart (α-$NaYF_4$/$NaYF_4$).[33] Subsequently, heterogeneous material combinations with CaF_2 have been reported by several groups, mostly for their biocompatibility.[44−47] Furthermore, the current authors recently demonstrated another critical advantage of heterogeneous material combinations between α-$NaYF_4$:Yb:Er:Ce and CaF_2 for the formation of a true core−shell structure, realizing a significant boost of the SWIR emission of Er^{3+} at ca. 1500 nm with an absolute PLQY of 50%.[32]

In this article, the effect of various homogeneous and heterogeneous material combinations on the downshifting emission of Tm^{3+} above 1600 nm ($^3F_4 \rightarrow {}^3H_6$ transition) is investigated. Both the cubic α-$NaTmF_4$ (space group $Fm\bar{3}m$) and tetragonal $LiTmF_4$ (space group $I4_1/a$) crystal structures are used as the optically active core domains and combined with various homogeneous (same crystal structure and similar chemical composition) and heterogeneous (different crystal structures and/or drastically different chemical compositions) anticipated inert shell domains. Advanced electron microscopy (EM) techniques combined with powder X-ray diffraction (PXRD) are implemented to finely characterize the structural and chemical organization of the synthesized homo- and heterostructured NCs. Although the latter are synthesized under the exact same growth conditions, huge differences regarding their true chemical organization are apparent, with a dramatic impact on the Tm^{3+} emission above 1600 nm. Indeed, depending on the type of material combination, the Tm^{3+} emission in the far end of the SWIR region can be totally quenched or highly efficient. Thus, the most efficient material combination ($LiTmF_4$/$LiYF_4$) exhibits a high PLQY for Tm^{3+} emission above 1600 nm, reaching 39% under 800 nm excitation for excitation power densities in the range of 0.5−3 W/cm^2. The latter are still higher than the permissible skin exposure limit defined by the European regulation (EN60825-1:2014), which is 0.32 W/cm^2 for exposure time from 10 to 3 × 10^4 seconds. The results reported here constitute a unique contribution to reveal how material combinations − initially selected and designed to give rise to the formation of true core−shell structures − can influence the spatial redistribution of optically active and optically inert elements with important consequences for Tm^{3+} SWIR emission. The results constitute a significant progress in the understanding of the structure−property relationships of RE-based core−shell NCs. It is anticipated that this will stimulate the emergence of a new era of optimizing the optical properties of homo- and heterostructured RE-based core−shell NCs, thus enabling them to rise to the challenge of highly efficient SWIR-emitting nanoprobes for *in vivo* imaging.

RESULTS AND DISCUSSION

Overview of the Investigated Material Combinations. An overview of the two different types of crystal structures (cubic and tetragonal) from which six different material combinations were derived for the synthesis of anticipated core/shell NCs together with useful ionic radii is given in Figure 1. For Tm^{3+} downshifting in the SWIR region, cubic α-$NaTmF_4$ (Figure 1a) and tetragonal $LiTmF_4$ (Figure 1b) were selected as the two different types of optically active core NCs. Note that the hexagonal structure (β-$NaTmF_4$) was excluded due to (i) the complexity of its crystal structure with a nontrivial site occupation frequency (SOF), which significantly complicates the structural investigations and (ii) its strong tendency to form alloys.[48] α-$NaYF_4$ (Figure 1a), CaF_2 (Figure 1a), and $LiYF_4$ (Figure 1b) were selected as protecting (i.e., optically inactive) shell materials. The main objective is to understand how material combinations influence the crystal structure and chemical organization of the final homo- and heterostructured NCs together with the consequences on the downshifting properties of Tm^{3+} above 1600 nm. Mechanistic investigations regarding the dynamics of shell growth for the different material combinations reported, although of interest, are beyond the scope of this article. Therefore, only static characterizations performed on the final products are reported. For a fair comparison, all material combinations were synthesized under the same experimental conditions (solvent,

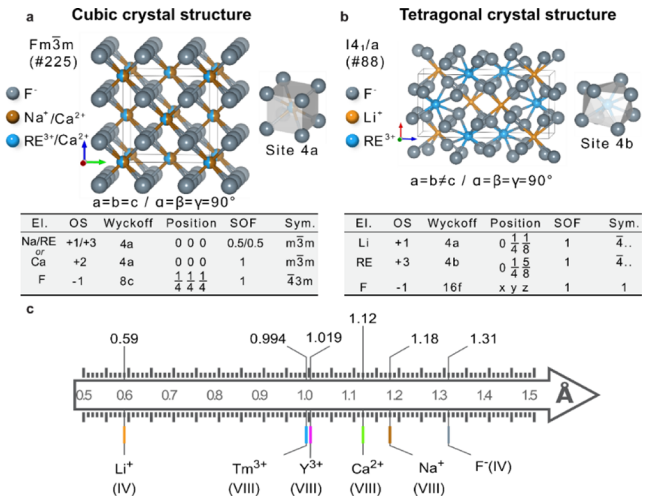

Figure 1. Selected crystal structures for homogeneous and heterogeneous material combinations. Cubic (a) and tetragonal (b) crystal structures from which six different material combinations were derived for the synthesis of anticipated core/shell nanocrystals. All six material combinations are described in the main text. For each crystal structure, the scheme of the corresponding unit cell is shown together with the symmetry of the metal site (RE = rare earth element, Tm or Y in this article). Tables underneath the unit cells summarize relevant crystallographic information such as the Wyckoff positions, atomic coordinates, site occupation frequencies (SOFs), and site symmetry. The ionic radii of all investigated cations (taken from Shannon)[49] are given for coordination numbers observed in the crystal structures of the selected materials (c).

capping agent, chemical precursors, shell precursor delivery, heating rate, aging time, and growth temperature) as detailed in the Supporting Information. Homogeneous material combinations refer to core and shell materials that exhibit the same crystal structure with a high probability of forming solid solutions, such as α-$NaTmF_4$/$NaYF_4$ (cubic/cubic) and $LiTmF_4$/$LiYF_4$ (tetragonal/tetragonal). On the contrary, heterogeneous material combinations refer to core and shell materials that exhibit different crystal structures and/or a limited capability to form solid solutions, including α-$NaTmF_4$/CaF_2 (cubic/cubic), α-$NaTmF_4$/$LiYF_4$ (cubic/tetragonal), $LiTmF_4$/$NaYF_4$ (tetragonal/cubic), and $LiTmF_4$/CaF_2 (tetragonal/cubic).

Material Combinations with Cubic α-$NaTmF_4$ Core NCs. *Structural Characterization of the Starting α-$NaTmF_4$ Core NCs.* The PXRD pattern of the synthesized α-$NaTmF_4$ core NCs reveals the formation of the expected cubic structure with no trace of secondary phases. Indeed, the experimental PXRD pattern (Figure 2a – black open symbols) is properly described when performing a Pawley refinement with a single cubic ($Fm\bar{3}m$) phase (Figure 2a – color solid line). The corresponding lattice parameter of the synthesized α-$NaTmF_4$ core NCs is 5.4762(2) Å. The Pawley refinement was performed by implementing the whole powder pattern modeling (WPPM) method with a spherical isotropic model,[50,51] which allows for an isotropic crystallite size (mean sphere diameter) of 9.1 ± 2.4 nm to be extracted. The latter value is in good agreement with the particle size distribution obtained by the analysis of high-angle annular dark-field transmission scanning electron microscopy (HAADF-STEM) images with a mean size of 8.6 ± 2.0 nm (Figure 2b,c). The synthesized α-$NaTmF_4$ NCs are utilized as the starting seeds for all material combinations with optically inactive α-$NaYF_4$, CaF_2, and $LiYF_4$.

Structural Characterization of Homogeneous and Heterogeneous Material Combinations with Cubic α-$NaTmF_4$ Core NCs. The homogeneous combination with $NaYF_4$ is a classical archetype widely reported in the literature. The PXRD pattern of α-$NaTmF_4$/$NaYF_4$ reveals the formation of two phases (Figure 3a). The cubic and hexagonal phases were quantified to be 99 and 1 wt %, respectively. Due to the minimal content of the hexagonal phase, it is neglected in the

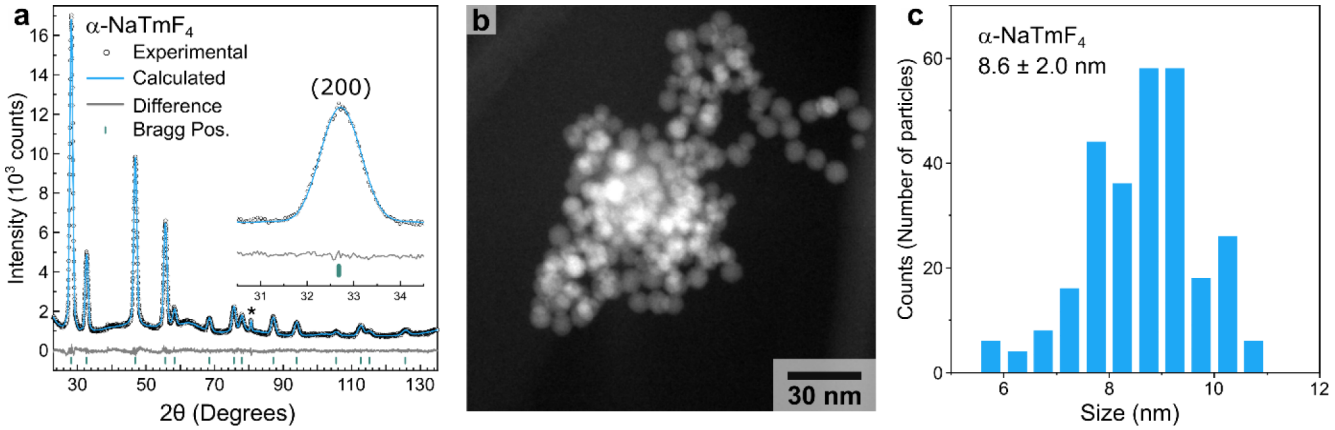

Figure 2. Structural characterization of the starting α-$NaTmF_4$ core nanocrystals (NCs) utilized as starting seeds for homogeneous and heterogeneous material combinations. Experimental (black open symbols) powder X-ray diffraction (PXRD) pattern and corresponding Pawley refinement (color solid line) (a). The difference between the experimental and calculated PXRD patterns is shown (gray solid line) together with Bragg peak positions (green vertical bars). Note that the peak identified with a star (*) at ca. 80° does not belong to the cubic crystal structure but to the low background (911)-oriented silicon wafer onto which NCs are drop casted (Figure S1). The peak is properly modeled because the signal of the empty low background (911)-oriented silicon wafer was utilized to define the background. The inset shows a magnification of the (200) reflection, the relevance of which is discussed in the main text. Representative low magnification high-angle annular dark-field scanning transmission electron microscopy (HAADF-STEM) image (b) and size distribution histogram (c). A minimum of 300 individual particles from different HAADF-STEM images were analyzed for the size distribution histogram. The standard deviation is given as two sigma (2σ).

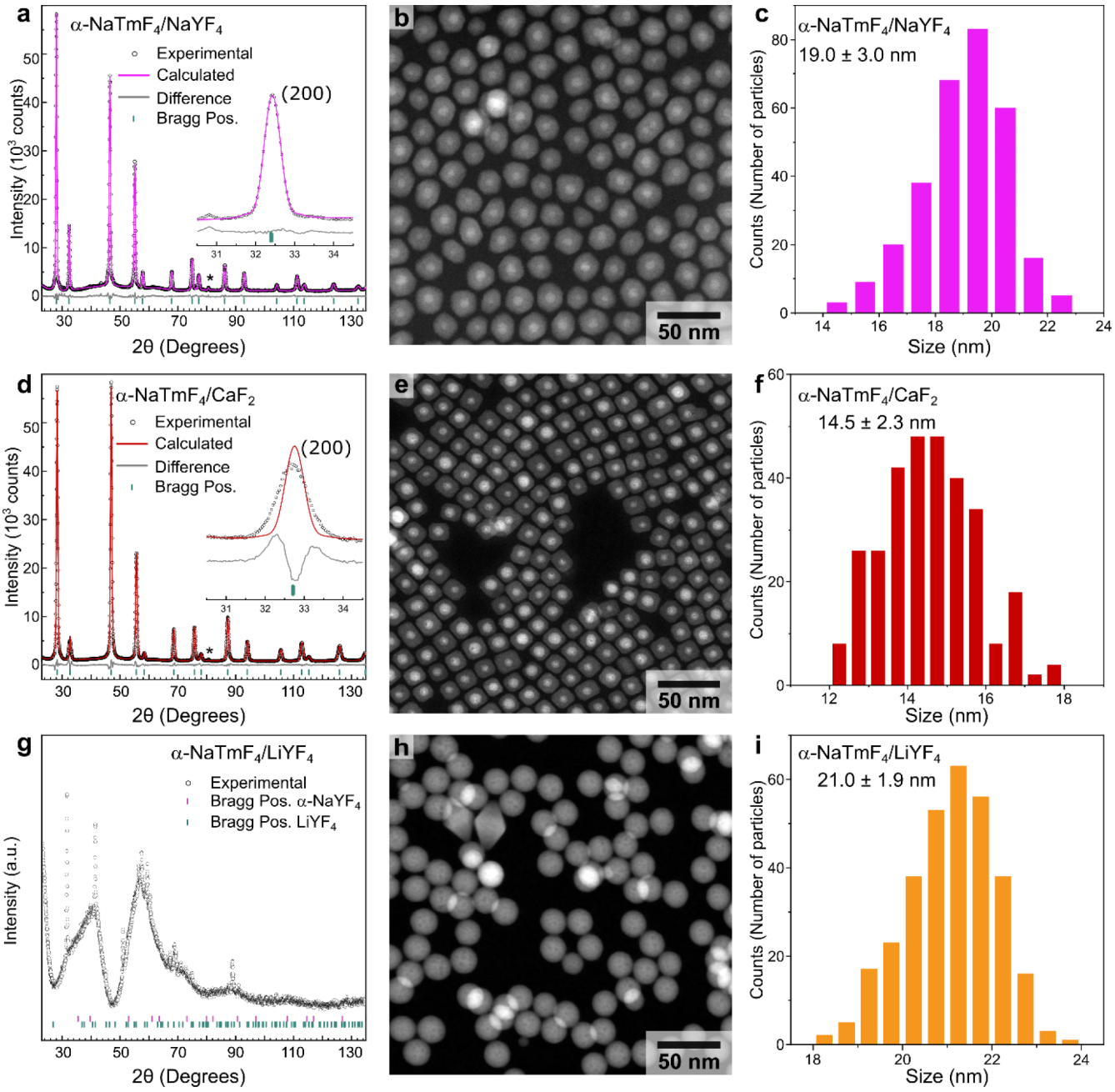

Figure 3. Structural characterization of material combinations of α-$NaTmF_4$ core nanocrystals (NCs) with cubic α-$NaYF_4$ (homogeneous combination – top row), cubic CaF_2 (heterogeneous combination – middle row), and tetragonal $LiYF_4$ (heterogeneous combination – bottom row). Experimental (black open symbols) powder X-ray diffraction (PXRD) patterns and corresponding Pawley refinements (color solid lines) (a, d, g). The Pawley refinements are shown only for the homogeneous ($NaYF_4$) and first heterogeneous (CaF_2) combinations. The difference between the experimental and calculated PXRD patterns is shown (gray solid lines) together with Bragg peak positions (green vertical bars). Note that the peak identified with a star (*) at ca. 80° does not belong to the cubic crystal structure but to the low background (911)-oriented silicon wafer onto which NCs are drop casted (Figure S1). The insets (a, d) show a magnification of the (200) reflection, the relevance of which is discussed in the main text. Representative low magnification high-angle annular dark-field scanning transmission electron microscopy (HAADF-STEM) images (b, e, h) and size distribution histograms (c, f, and i). A minimum of 300 individual particles were analyzed from different HAADF-STEM images for each size distribution histogram. The standard deviation is given as two sigma (2σ).

analysis. Bragg peaks of the cubic phase (Figure 3a – black open symbols) are significantly sharper compared to the pure α-$NaTmF_4$ core NCs (Figure 2a). The corresponding Pawley refinement (Figure 3a – color solid line) indicates a larger lattice parameter (a = 5.52194 (13) Å) compared to the starting core NCs. The isotropic size of the coherent domains (WPPM approach, isotropic model) clearly increases compared with the starting core, reaching 21.4 ± 1.6 nm. The overview HAADF-STEM image (Figure 3b) shows the formation of isotropic particles with a subtle but clearly visible contrast between the inner and outer regions of the particles. The extracted overall size distribution histogram (Figure 3c) yields a mean size of 19.0 ± 3.0 nm, which is in relatively good agreement with the PXRD measurements. Despite the poor

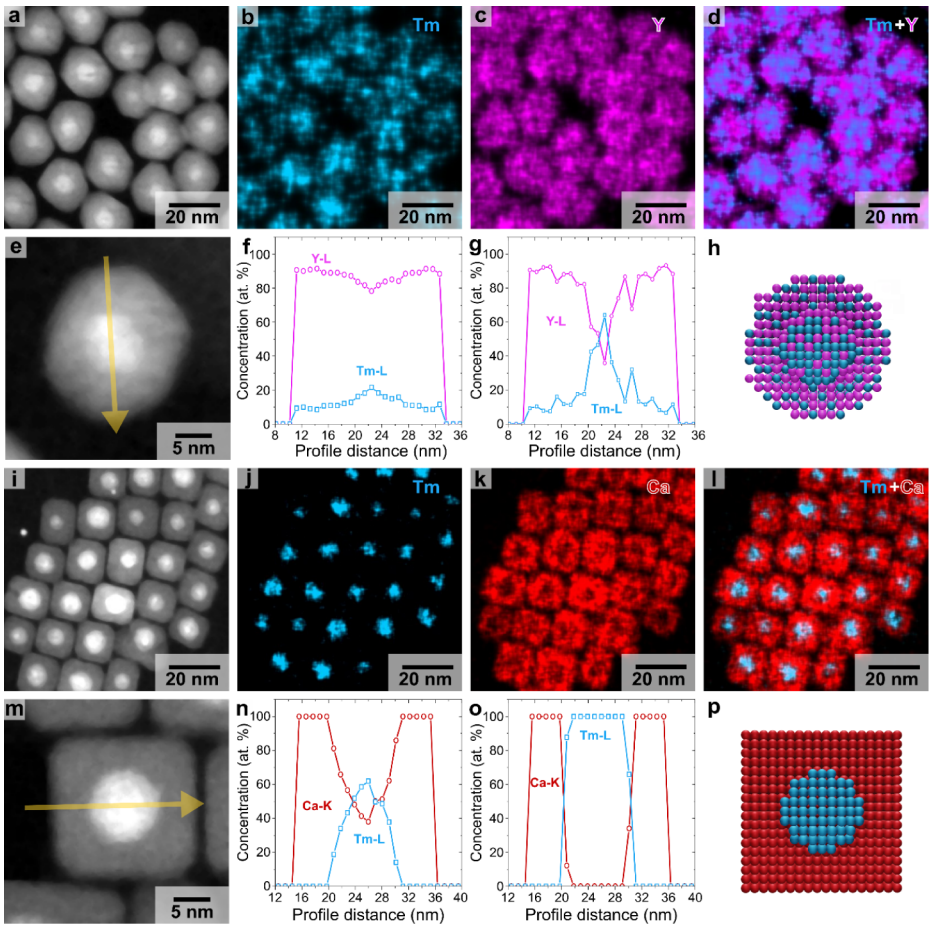

Figure 4. Chemical analyses of material combinations of α-$NaTmF_4$ core nanocrystals (NCs) with cubic α-$NaYF_4$ (homogeneous combination – first and second rows) and cubic CaF_2 (heterogeneous combination – third and fourth rows). High-angle annular dark-field scanning transmission electron microscopy (HAADF-STEM) images of the energy dispersive X-ray (EDX) spectroscopy mapping areas (a, i) and corresponding Tm (Tm-L_α line) (b, j), Y (Y-L line) (c), and Ca (Ca–K_α line) (k) chemical maps together with their overlap (d, l) for the homogeneous (a–-d) and heterogeneous (i–-l) material combinations. HAADF-STEM images of single particles for homogeneous (e) and heterogeneous (m) material combinations on which EDX line-scan (yellow arrows) analyses were performed. Normalized raw (f, n) and calculated (subshell approach) (g, o) chemical profiles obtained for the homogeneous (e–-g) and heterogeneous (m–-o) material combinations. Qualitative scheme illustrating the most probable distribution of cations for the homogeneous (h) and heterogeneous (p) material combinations. Tm, Y, and Ca are represented in blue, magenta, and red, respectively.

contrast difference between the inner and outer regions, it was possible to obtain the size distribution histogram of the brighter "core" region only (Figure S2). Although the accuracy is limited due to the poor contrast, it is obvious that the corresponding "core only" histogram is shifted toward the smaller size range.

The PXRD pattern of the first heterogeneous combination with CaF_2 (α-$NaTmF_4$/CaF_2) indicates the formation of a unique cubic phase with no trace of secondary phases (Figure 3d – black open symbols). It is important to emphasize that, despite the larger size of Ca^{2+} ($rCa^{2+}_{(VIII)}$ = 112 pm) compared to Y^{3+} ($rY^{3+}_{(VIII)}$ = 102 pm), the Pawley refinement (Figure 3d – color solid line) indicates a nearly unchanged lattice parameter (a = 5.47068(13) Å) compared to the starting core NCs, while the size of the coherent domains (WPPM approach, isotropic model) increases up to 16.4 ± 5.0 nm.

It is worth noting that contrary to the core NCs (α-$NaTmF_4$) and homogeneous material combination (α-$NaTmF_4$/$NaYF_4$), the Pawley refinement is not able to properly model specific Bragg reflections such as (200) (Figure 3d – inset), (222), (420), and (600). That particular point will be treated later in the text (see the dedicated section "*Focus on diffraction data*"). The HAADF-STEM image shows the formation of monodisperse cubes with rounded corners (Figure 3e). Additionally, a pronounced contrast difference between the inner and outer regions of the particles is clearly visible. The extracted overall size distribution histogram (Figure 3f) exhibits a mean size of 14.5 ± 2.3 nm, in agreement with the crystallite size obtained from X-ray diffraction. The pronounced contrast difference between the inner and outer regions of the particles can easily be used to extract an accurate size distribution histogram (Figure S3) of the brighter "core" region only, which is in very good agreement with the size distribution histogram of the starting core NCs (Figure 2c).

The PXRD pattern of the second heterogeneous combination with $LiYF_4$ (α-$NaTmF_4$/$LiYF_4$) shows uncommon features with extremely broad peaks (several tens of degrees) together with relatively sharp peaks (Figure 3g). The origin of the broad peaks is very likely a legacy of the original α-$NaTmF_4$ cubic phase, which is completely fragmented into very small crystallites within the tetragonal phase. Indeed, the

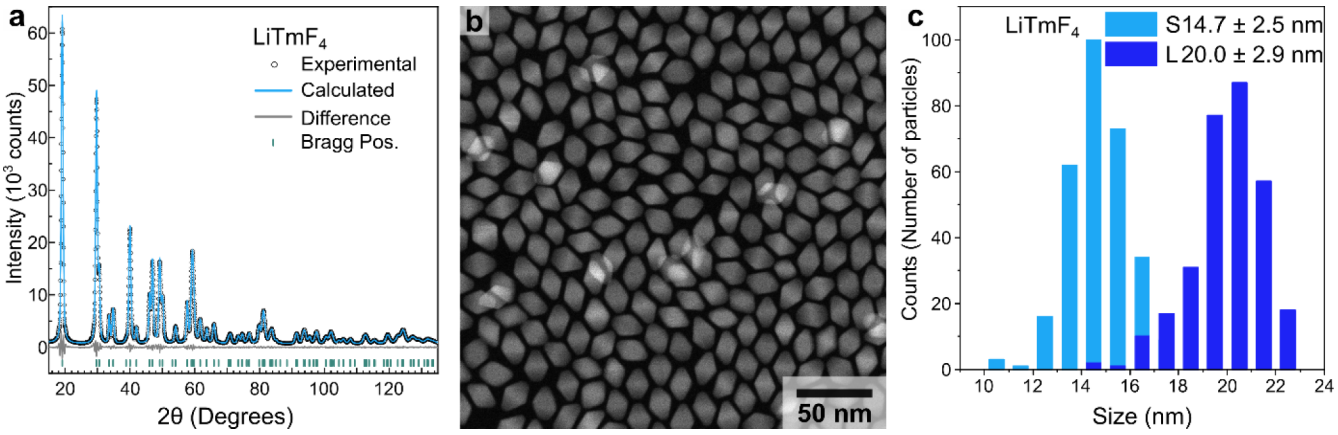

Figure 5. Structural characterization of the starting $LiTmF_4$ core nanocrystals (NCs) utilized as starting seeds for homogeneous and heterogeneous material combinations. Experimental (black open symbols) powder X-ray diffraction (PXRD) pattern and corresponding Pawley refinement (color solid line) (a). The difference between the experimental and calculated PXRD patterns is shown (gray solid line) together with Bragg peak positions (green vertical bars). Representative low magnification HAADF-STEM image (b) and size distribution histogram (c). As anisotropic particles are obtained, size distribution histograms for both the short (S) and long (L) axes are given. A minimum of 300 individual particles from different HAADF-STEM images were analyzed for the size distribution histograms. The standard deviation is given as two sigma (2σ).

sharper peaks match the formation of the tetragonal phase $LiYF_4$. The corresponding overview HAADF-STEM image supports the "fragmentation" of the original core domain with a highly homogeneous contrast throughout the individual particles (Figure 3h). The latter are mostly spherical with a mean size of 21.0 ± 1.9 nm (Figure 3i). Because of the complete alloying, the heterogeneous material combination α-$NaTmF_4/LiYF_4$ was not further investigated regarding its structural characterization.

Chemical Organization of Material Combinations with Cubic α-$NaTmF_4$ Core NCs. Chemical maps obtained by energy-dispersive X-ray (EDX) spectroscopy, with spatial resolution down to the nanometer scale, provide a facile means of obtaining a first insight into the spatial distribution of cations in homogeneous (α-$NaTmF_4/NaYF_4$) and heterogeneous (α-$NaTmF_4/CaF_2$) material combinations. The EDX chemical maps of Tm (Tm-L_α line) are of particular interest because Tm is supposed to be confined only in the core domain for both the homogeneous and heterogeneous material combinations. Consequently, any change in the Tm distribution can be unambiguously determined by analyzing its EDX chemical maps. This is more challenging for the chemical elements that are supposed to be confined in the shell domains, such as Y (homogeneous combination) and Ca (heterogeneous combination), which also surround the Tm core domain. A clear difference is visible between the EDX maps of Tm for the homo- (Figure 4a,b) and heterostructured (Figure 4i,j) NCs. Indeed, the Tm distribution is more diffuse in the former compared to that in the latter. Additionally, subtle but real differences are also visible when inspecting the EDX maps of the shell elements Y (Y-L line) (homogeneous combination only, Figure 4c) and Ca (Ca−K_α line) (heterogeneous combination only, Figure 4k). In the latter case, dark voids are visible, and their spatial localization is in agreement with the strongly localized spatial distribution of Tm. This effect (i.e., void formation) is nearly nonexistent in the case of Y distribution (Figure 4c) for the homogeneous material combination. Interestingly, the superposition of the EDX maps of the core-confined and shell-confined elements suggests, to a certain extent, the formation of an alloy for the homogeneous material combination (Figure 4d). On the contrary, for the heterogeneous material combination (Figure 4l), the formation of particles with a true core−shell organization is very probable.

Chemical mapping can be refined by separately recording and analyzing independent EDX line-scans. Indeed, chemical concentration profiles are obtained by the quantification of EDX spectra recorded along a line that passes through the center of the analyzed particle with probe and step sizes of 0.25 and 1 nm, respectively.

Although not performed on a whole particle but only through a single line crossing the analyzed particle, chemical information (along that line) with a local precision of ca. 1 nm can be obtained. At this point, it is important to emphasize that the quantification of EDX spectra recorded during line-scan analysis leads to the determination of "overlapped" chemical concentration profiles, which are averaged along the electron-beam direction. Thus, a mathematical treatment of the obtained raw chemical concentration profiles must be implemented to obtain the localized chemical composition corrected from the outermost "subshell" domain contribution. It is worth noting that such a mathematical procedure, known as the subshell approach[1,52] is sensitive not only to the overall shape of the particle but also to the shape of the buried core domain. Consequently, quasi-spherical/elliptical core and shell geometries have been used for the homogeneous material combination (α-$NaTmF_4/NaYF_4$) while quasi-spherical core geometry and cubic shell geometry have been used for the heterogeneous material combination (α-$NaTmF_4/CaF_2$).[32] Even if the utilized core and shell geometries in the subshell approach are ideal ones, they constitute relatively good approximations of the real shapes. Finally, to deal not only with deviations from ideal geometries but also with the orientation of the particle relative to the incident electron-beam, at least ten particles are analyzed for each material combination.

The normalized raw chemical profiles (i.e., before mathematical treatment) of Tm (Tm-L series) and Y (Y-L series) obtained for the homogeneous material combination (α-$NaTmF_4/NaYF_4$, Figure 4e) demonstrate the presence of

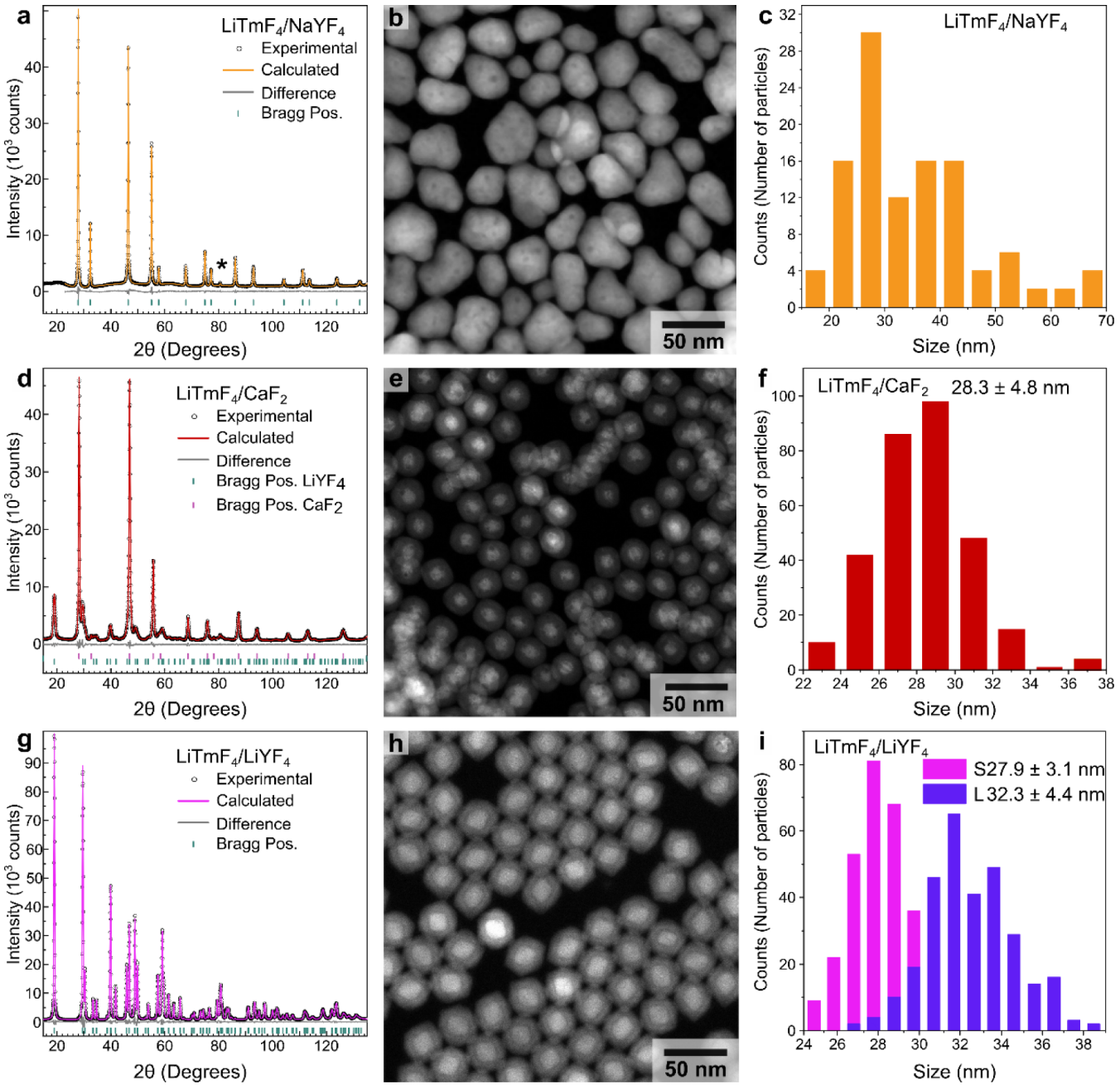

Figure 6. Structural characterization of material combinations of $LiTmF_4$ core nanocrystals (NCs) with cubic α-$NaYF_4$ (heterogeneous combination – top row), cubic CaF_2 (heterogeneous combination – middle row), and tetragonal $LiYF_4$ (homogeneous combination – bottom row). Experimental (black open symbols) powder X-ray diffraction (PXRD) patterns and corresponding Pawley refinements (color solid lines) (a, d, g). The difference between the experimental and calculated PXRD patterns is shown (gray solid lines) together with Bragg peak positions (green vertical bars). In the case of the heterogeneous material combination $LiTmF_4/CaF_2$, two sets of Bragg peak positions are requested for the tetragonal (green vertical bars) and cubic (pink vertical bars) phases. Note that the peak identified with a star (*) at ca. 80° does not belong to the cubic crystal structure but to the low background (911)-oriented silicon wafer onto which NCs are drop casted (Figure S1). Representative low magnification high-angle annular dark-field scanning transmission electron microscopy (HAADF-STEM) images (b, e, h) and size distribution histograms (c, f, i). A minimum of 300 individual particles from different HAADF-STEM images were analyzed for each size distribution histogram. The standard deviation is given as two sigma (2σ).

Tm well beyond the spatial limits of the core region as it is detected until the edges of the particle (Figure 4f). This is in perfect agreement with the EDX map of Tm (Figure 4b). When applying the subshell approach to the raw normalized concentration profiles of Tm and Y, a fully alloyed NC with concentration gradients is revealed (Figure 4g,h). It is important to emphasize that neither pure core nor pure shell domains are detected for the homogeneous material combination. This is in distinct contrast with the Tm and Ca chemical profiles calculated after applying the subshell approach for the heterogeneous material combination (α-$NaTmF_4/CaF_2$, Figure 4m), which are in perfect agreement with the formation of a true core–shell structure (Figure 4n–p) with pure Tm-core and Y-shell regions. This supports the

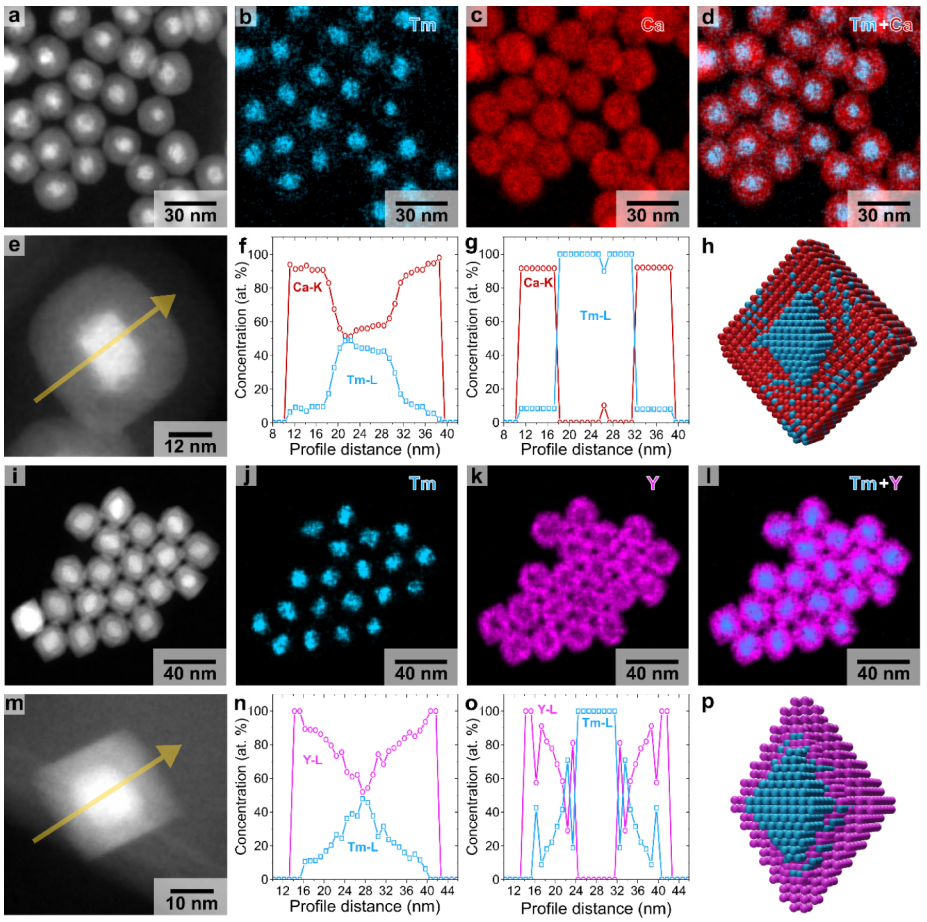

Figure 7. Chemical analyses of material combinations of $LiTmF_4$ core nanocrystals (NCs) with cubic CaF_2 (heterogeneous combination – first and second rows), and tetragonal $LiYF_4$ (homogeneous combination – third and fourth rows). High-angle annular dark-field scanning transmission electron microscopy (HAADF-STEM) images of the energy dispersive X-ray (EDX) spectroscopy mapping areas (a, i) and corresponding Tm (Tm-L_α line) (b, j), Ca (Ca–K_α line) (c), and Y (Y-L line) (k) chemical maps together with their overlap (d, l) for the heterogeneous (a–-d) and homogeneous (i–-l) material combinations. HAADF-STEM images of single particles of heterogeneous (e) and homogeneous (m) material combinations on which EDX line scan (yellow arrows) analyses were performed. Normalized raw (f, n) and calculated (subshell approach) (g, o) chemical profiles obtained for the heterogeneous (e–-g) and homogeneous (m-–o) material combinations. Scheme illustrating the most probable qualitative distribution of cations for the heterogeneous (h) and homogeneous (p) material combinations. Tm, Y, and Ca are colored blue, magenta, and red, respectively.

qualitative results from EDX mapping (Figure 4j–l). Additional EDX line scans treated with the subshell approach are available in the Supporting Information (Figures S4 and S5).

Material Combinations with Tetragonal $LiTmF_4$ Core NCs. *Structural Characterization of the Starting $LiTmF_4$ Core NCs.* The PXRD pattern of the synthesized $LiTmF_4$ core NCs reveals the formation of the expected tetragonal structure with no trace of secondary phases. Indeed, the experimental PXRD pattern (Figure 5a – black open symbols) is properly described when performing a Pawley refinement with a single tetragonal ($I4_1/a$) phase (Figure 5a – color solid line). The corresponding lattice parameters of the synthesized $LiTmF_4$ core NCs are 5.14971(15) Å (a and b parameters) and 10.6507(4) Å (c parameter). The Pawley refinement was performed by applying an elliptical anisotropic model with the double Voigt approach.[53] The latter allows to extract an anisotropic crystallite size of 14.6 ± 1.8 nm and 19.4 ± 2.1 nm for the short and long axes, respectively. These values are in perfect agreement with the particle size distribution obtained by the analysis of HAADF-STEM images with mean sizes of 14.7 ± 2.5 nm and 20.0 ± 2.9 nm for the short axis and long axis, respectively (labeled S and L in Figure 5c). The synthesized $LiTmF_4$ NCs are utilized as the starting seeds for all material combinations with α-$NaYF_4$, CaF_2, and $LiYF_4$.

Structural Characterization of Homogeneous and Heterogeneous Material Combinations with Tetragonal $LiTmF_4$ Core NCs. The PXRD pattern of the first heterogeneous material combination with $NaYF_4$ ($LiTmF_4/NaYF_4$) indicates the formation of a unique cubic phase ($Fm\bar{3}m$) with no remaining trace of the initial tetragonal phase (Figure 6a – black open symbols). The corresponding Pawley refinement (Figure 6a – color solid line) indicates a lattice parameter of the cubic phase of 5.52321(8) Å. The isotropic size of the coherent domains (WPPM approach, isotropic model) clearly increases compared to the starting core to reach 26.4 ± 8.7 nm. The PXRD pattern analysis shows that the structural integrity of the starting core NCs has been completely destroyed. The corresponding overview HAADF-STEM image supports the total destruction of the original core NCs with a highly homogeneous contrast throughout individual particles (Figure 6b). The latter exhibit nonuniform and irregular shapes with a very broad size distribution (Figure 6c) in agreement with PXRD results. Because of the complete alloying, the first

heterogeneous material combination $LiTmF_4/NaYF_4$ was not further investigated regarding its structural characterization.

Interestingly, the PXRD pattern of the second heterogeneous combination with CaF_2 ($LiTmF_4/CaF_2$) reveals the coexistence of both the initial tetragonal phase together with a new cubic ($Fm\bar{3}m$, $a = b = c = 5.46485(11)$ Å) phase (Figure 6d − black open symbols). The corresponding Pawley refinement (Figure 6d − color solid line) indicates slight modifications of the lattice parameters of the tetragonal phase ($a = b = 5.1704(5)$ Å, $c = 10.641(2)$ Å) compared to the starting core NCs. The corresponding HAADF-STEM image indicates the formation of isotropic NCs with a clear contrast difference between the core and shell domains (Figure 6e). The extracted size distribution histogram (Figure 6f) indicates the formation of larger particles (compared to the starting core NCs) with a mean size of 28.3 ± 4.0 nm. The marked contrast difference between the inner and outer regions can easily be used to extract a size distribution histogram (Figure S6) of the brighter "core" region only. Similar to the starting $LiTmF_4$ core NCs, the bright regions exhibit a slightly anisotropic shape. Both the short and long axes are slightly shorter compared to the starting core NCs (Figure 5c), which indicates a modification of the starting core domain.

The PXRD pattern of the homogeneous combination with $LiYF_4$ ($LiTmF_4/LiYF_4$) reveals the formation of a single tetragonal phase with no sign of secondary phases (Figure 6g). Bragg peaks of the tetragonal phase (Figure 6g − black open symbols) are significantly sharper compared to the starting $LiTmF_4$ core NCs (Figure 5a). The corresponding Pawley refinement (Figure 6g − color solid line) indicates a larger c lattice parameter (10.7105(3) Å) compared to the starting $LiTmF_4$ core NCs while the a and b lattice parameters are very similar (5.16385(10) Å). The size of the coherent domains (WPPM approach, isotropic model) increases compared to the starting core NCs to reach 29.6 ± 2.5 nm. The HAADF-STEM image shows the formation of slightly anisotropic particles with a subtle but distinguishable contrast difference between the inner and outer regions of the particles (Figure 6h). The extracted size distribution histogram (Figure 6i) is in relatively good agreement with PXRD measurements with a mean size of 27.9 ± 3.1 nm and 32.3 ± 4.4 nm for the short and long axes, respectively. The relatively good contrast difference between the inner and outer regions can easily be used to extract an accurate size distribution histogram (Figure S7) of the brighter "core" region only. Although the size of the short axis (14.3 ± 2.5 nm) is in good agreement with the starting core NCs (Figure 5c), it is obvious that the size of the long axis (16.9 ± 2.6 nm) is shorter compared to the starting core NCs (Figure 5c).

Chemical Organization of Material Combinations with Tetragonal $LiTmF_4$ Core NCs. EDX chemical mapping shows that the Tm (Tm-L_α line) distribution is localized in the anticipated core region with signs of diffusion into the shell region both for the heterogeneous (Figure 7a,b) and homogeneous (Figure 7i,j) material combinations with $LiTmF_4$ core NCs. Interestingly, the Tm distribution appears to be more confined in the case of the homogeneous combination compared to its heterogeneous counterpart, which is in opposition to the observation made for material combinations with cubic α-$NaTmF_4$ core NCs (Figure 4). It is worth noting that despite the highly concentrated Tm distribution in the core region of the heterogeneous material combination, a secondary Tm distribution with a much lower intensity is also visible in the shell domain. The corresponding speckled Tm distribution extends within the entire volume of the particles. Although a similar behavior is observed for the homogeneous material combination, Tm does not reach the outermost regions of the particles. The EDX maps of the distribution of the shell elements Ca (Ca−K_α line) (heterogeneous combination only, Figure 7c) and Y (Y-L line) (homogeneous combination only, Figure 7k) exhibit the formation of dark voids in the innermost regions of the particles, whose spatial localization is in agreement with the main spatial distribution of Tm. Interestingly, the superposition of the EDX maps of the core-confined and shell-confined elements suggests the formation of core−shell structures both for the heterogeneous (Figure 7d) and homogeneous (Figure 7l) combinations. Nevertheless, the superposition of the EDX maps shows that no pure shell domain (i.e., Ca only) is formed for the heterogeneous material combination (Figure 7d) contrary to the homogeneous material combination (Figure 7l) for which a thin (ca. 2−3 nm) pure Y region is formed at the outermost regions of the particles.

The normalized raw chemical profile of Tm (Tm-L series) obtained for a single homostructured NC ($LiTmF_4/LiYF_4$, Figure 7m) reveals the presence of Tm well beyond the spatial limits of the starting core NCs but without being detected at the edges (Figure 7n). When applying the subshell approach with bipyramidal core and shell geometries (Supporting Information) to the raw EDX chemical profiles of Tm and Y (Y-L series), a true core−shell structure is revealed (Figure 7o,p). Nevertheless, although the existence of pure core ($LiTmF_4$ with a size of about 8−9 nm) and pure shell ($LiYF_4$ with a thickness of about 2−3 nm) domains is not questionable, a thick (ca. 10 nm) interfacial layer is observed, which is in agreement with EDX maps. Thus, $LiTmF_4$ and $LiYF_4$ coexist with a third crystalline (tetragonal) interphase, which is a nonhomogeneous alloy ($LiTm_{1-x}Y_xF_4$) with concentration gradients (i.e., different values for x depending on the spatial location within the interphase) in between the pure core and pure shell domains. The "spiky" aspect of the concentration profile of Tm (Figure 7o) was observed for all particles investigated for this material combination. It is probably caused by the relatively large fluctuation for the gradient in the intermixing regions and the deviation of the real structure from the ideal model used in the subshell analysis. Note that the Tm concentrations determined for the outermost regions of the core domain are characterized by larger errors compared to all other Tm concentrations measured along the EDX line scan due to a thickness effect at the tips of the bipyramid.

The normalized raw chemical profile of Tm obtained for a single heterostructured NC ($LiTmF_4/CaF_2$, Figure 7e) confirms the presence of Tm well beyond the spatial limits of the core region until the outermost edges of the particle (Figure 7f).

The subshell approach with idealized bipyramidal core and cubic shell geometries (Supporting Information) was applied to the raw EDX chemical profiles of Tm and Ca and demonstrates the formation of a core−shell structure (Figure 7g,h). Nevertheless, contrary to its homogeneous counterpart, and although a pure core region is observed, the whole shell domain is doped with a constant concentration of Tm (ca. 8 at. %), indicating the formation of a homogeneous Tm-doped shell. The presence of Tm in the shell region detected by EDX

https://doi.org/10.1021/acsnano.4c07932
ACS Nano 2024, 18, 26233−26250

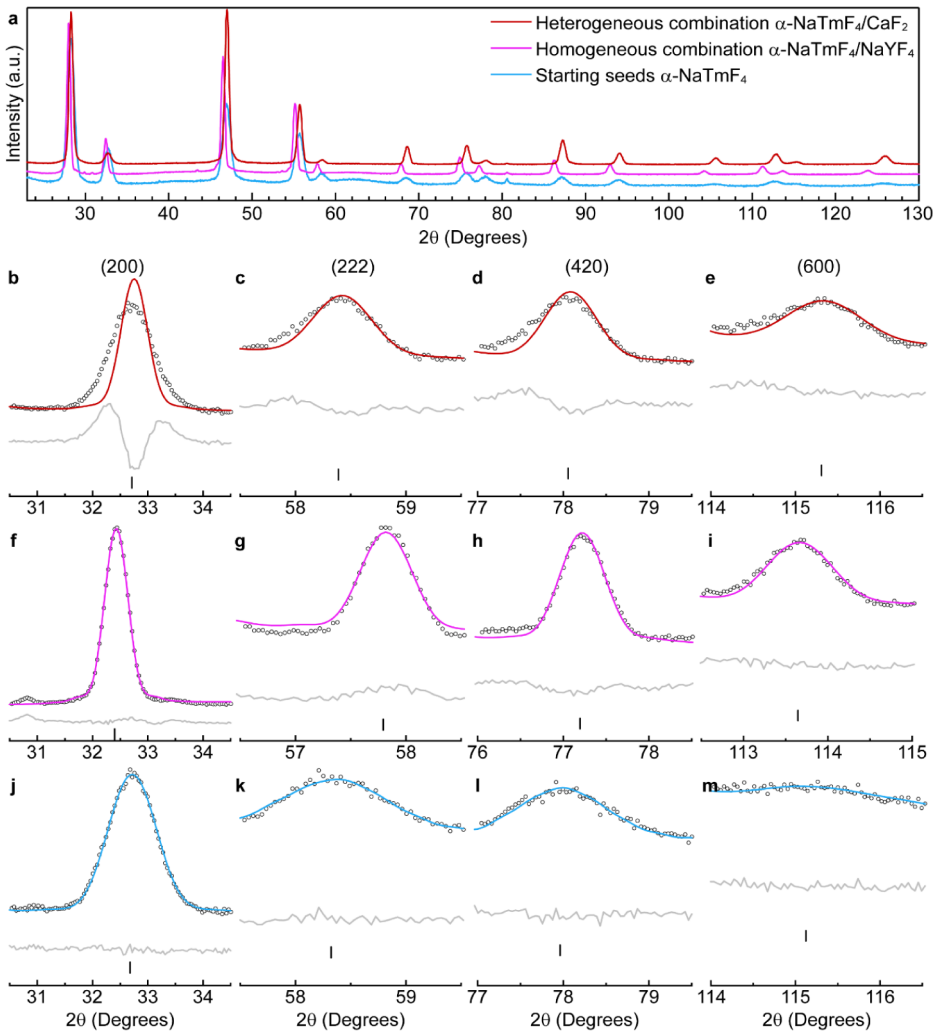

Figure 8. Comparison of PXRD data for homogeneous and heterogeneous material combinations with cubic α-$NaTmF_4$ core nanocrystals (NCs). (a) Experimental PXRD patterns of α-$NaTmF_4$ core NCs (blue solid line), homogeneous α-$NaTmF_4/NaYF_4$ (magenta solid line), and heterogeneous α-$NaYF_4/CaF_2$ (red solid line) material combinations. (b−-m) Experimental (black open symbols) and calculated (color solid lines) peak profiles for the (200), (222), (420), and (600) Bragg reflections. Data of individual Bragg reflections are given for α-$NaTmF_4$ core NCs (first row from the bottom), homostructured α-$NaTmF_4/NaYF_4$ (second row from the bottom), and heterostructured α-$NaYF_4/CaF_2$ (third row from the bottom) NCs.

line-scan analysis confirms the interpretation of the EDX map of Tm (Figure 7b) and is corroborated by additional EDX line scans (Figure S8) as well as by the Rietveld refinement of the corresponding PXRD pattern. Indeed, the refinement of the SOF of the Ca site (Wyckoff position 4a) indicates a substitution of Ca by Tm of up to 7 at. %. The doping of the CaF_2 shell by Tm is further confirmed when analyzing the two-dimensional Fourier transform (FT) pattern of the high-resolution transmission electron microscopy (HRTEM) image of the outermost shell region (see dedicated section "*Focus on diffraction data*").

Focus on Diffraction Data. In the previous sections dedicated to material combinations with cubic α-$NaTmF_4$ or tetragonal $LiTmF_4$ core NCs, experimental evidence of the formation of alloyed or core−shell (with or without intermixing) structures was based on the utilization of EDX spectroscopy techniques (chemical maps and line scan analysis). Interestingly, for certain material combinations (e.g., α-$NaTmF_4/CaF_2$), a detailed inspection of the PXRD pattern revealed interesting features. The latter, when not performing proper refinements (in our case Pawley refinement), can easily pass unnoticed or be simply overlooked. Despite peak broadening due to the small size of the coherently diffracting domains, PXRD patterns of NCs are still of major interest when particular features can be exploited to extract useful structural information.

Compared to the starting cubic seeds (α-$NaTmF_4$), all Bragg peaks of the homogeneous combination (α-$NaTmF_4/NaYF_4$) are shifted toward lower two theta angles while Bragg peaks of the heterogeneous combination (α-$NaTmF_4/CaF_2$) remain almost unchanged (Figure 8a). This indicates that very likely differences exist in the microstructure (i.e., atomic-scale organization) of the two different combinations (homogeneous vs heterogeneous). Indeed, materials used for the homogeneous and heterogeneous combinations not only are isostructural polymorphs ($Fm\bar{3}m$) but also possess nearly identical lattice parameters. Thus, if the final atomic-scale organization of the two material combinations was equivalent, the same features should be observed for both the PXRD

https://doi.org/10.1021/acsnano.4c07932
ACS Nano 2024, 18, 26233−26250

patterns of the homogeneous and heterogeneous combinations.

The modification of the atomic-scale organization depending on the material combination is strengthened especially as the profile of some specific reflections − namely (200), (222), (420), and (600) − is successfully modeled for the core (Figure 8 − first row from the bottom) and homostructured (Figure 8 − second row from the bottom) NCs, but not for the heterostructured (Figure 8 − third row from the bottom) NCs. Such features (Bragg peaks shifting combined with the modified line profile of specific Bragg reflections) constitute interesting X-ray diffraction hallmarks to differentiate between alloying and phase segregation.

To verify our hypothesis, Debye's scattering equation was used to calculate the theoretical diffraction pattern of various atomistic models for a single NC.[54,55] In the case of a single isotropic NC of CaF_2 ($Fm\bar{3}m$) with a size of 21.8 nm (namely 40 unit cells), the theoretical diffraction pattern shows that intensities of the (200), (222), (420), and (600) reflections are equal to or very close to zero (Figure S9). On the contrary, when Ca is replaced by Tm in the atomistic model of the single NC, intensities of the (200), (222), (420), and (600) reflections are clearly different from zero (Figure S10). Consequently, as the nonzero intensity of specific Bragg peaks ((200), (222), (420), (600)) of the cubic crystal structure is fully dominated by the presence of Tm atoms, such Bragg peaks can be used to determine whether the underlying atomic-scale organization is compatible with alloying or phase segregation. The (200) reflection is particularly interesting because it is located at a low two theta angle (ca. 32.5°) with the highest relative intensity and no peak overlap compared to the (222), (420), and (600) reflections. As previously indicated (see section "α"), the Pawley refinement (with a single crystal structure) of the experimental PXRD pattern of the heterogeneous combination (α-$NaTmF_4/CaF_2$) fails to properly model the line profile of the (200), (222), (420), and (600) reflections, although it is adapted to all other reflections. It is important to emphasize that the calculated line profile of the (200) reflection is too narrow compared to the one experimentally observed. As the observation of the (200) reflection in the PXRD pattern is exclusively related to the presence of Tm within the diffracting domain, the discrepancy between the calculated and experimental line profiles can now be explained. Indeed, the size of the coherently diffracting domain within which Tm is confined is significantly smaller compared to the overall crystallite size. As the latter is in good agreement with the mean size obtained by HAADF-STEM, it confirms the structural coherence of the Ca domain throughout the entire particle even if Ca is absent from the core domain. Thus, the experimental PXRD pattern of the heterostructured NCs not only reflects the size of the Tm domain but also the size of the entire coherently diffracting domain, which includes both the Tm and Ca regions. Simulations showed that it is impossible to understand the overall line profile as a convolution of separate core and shell contributions. On the contrary, simulations with a perfect coherence between the core and shell domains can explain the observed line profile (Figure S11). Interestingly, the results obtained by advanced PXRD data analysis can be independently validated by the analysis of HRTEM data.

The HRTEM image of a single α-$NaTmF_4/CaF_2$ NC (Figure 9 − top row) confirms, in the direct space, the structural coherence of the entire NC. As expected, all

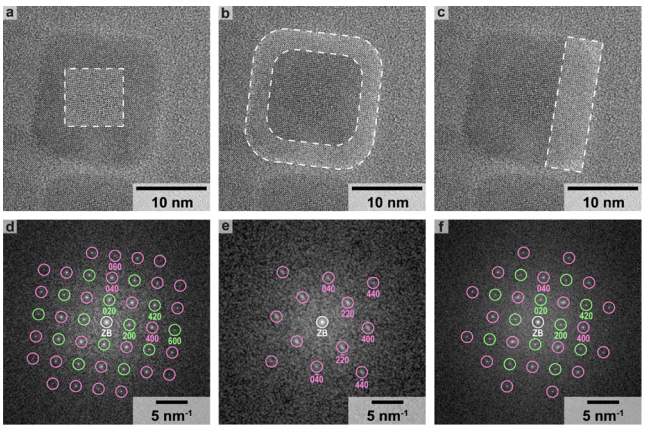

Figure 9. High resolution transmission electron microscopy (HRTEM) data for the heterogeneous material combination α-$NaTmF_4/CaF_2$. HRTEM images (a−c) and the two-dimensional Fourier transforms (FTs) of the highlighted dashed area (shown on the associated HRTEM image) together with their corresponding indexation. HRTEM images are the exact same, but different areas of the same particle were analyzed such as the inner region (a, d), the outermost (ca. 3−4 nm) shell (b, e), and a thicker region (ca. 5 nm) of the external shell (c, f). All corresponding FTs can be indexed with a cubic crystal structure ($Fm\bar{3}m$) in the [001] zone axis. For better readability of the two-dimensional FTs, the indices of only a small number of reflections are reported. Indices of all other reflections can be deduced from the indexed reflections and by symmetry. The zero-order beam (ZB) is marked with a white circle. All reflections marked with a pink or green circle belong to the cubic crystal structure ($Fm\bar{3}m$). Reflections marked with a green circle are characterized by a structure factor $|F_{(hkl)}|$ close to or equal to zero in the case of pure CaF_2 and should not be observed.

reflections (highlighted by pink and green circles) of the FT pattern of a central region (Figure 9a,d) of the NC can be indexed with a cubic crystal structure (space group $Fm\bar{3}m$). As in the case of PXRD, simulations have shown that the structure factor $|F_{(hkl)}|$ of certain reflections (highlighted by green circles on the FT pattern) is close to or equal to zero for pure CaF_2 but different from zero when Ca is substituted by Tm (ca. 5 at. % or higher). As the FT pattern of the central region (Figure 9d) is a superposition of the FT patterns of the core and shell domains, it is normal to observe all reflections. On the contrary, the FT pattern of the outermost 3−4 nm shell region is characterized by the absence of specific reflections, and in particular the (200), which is in perfect agreement with the formation of pure CaF_2 (Figure 9b,e). This nicely validates the conclusion derived from the analysis of the nonhomogeneous peak broadening observed for specific Bragg reflections on the PXRD pattern of α-$NaTmF_4/CaF_2$ NCs (Figure 8b−e). To demonstrate the sensitivity of the method, the FT pattern of a thicker (ca. 5−6 nm) outermost shell region was also obtained. As in the case of the central region, the "forbidden" reflections are visible (Figure 9c,f). This is expected because the thickness of the analyzed region (Figure 9c) is larger than the thickness of the pure CaF_2 shell as determined by EDX analysis (Figure 4n,o). Therefore, the corresponding FT pattern (Figure 9c) is a superposition of the FT patterns of the pure CaF_2 shell and α-$NaTmF_4$ core domains. The exact same strategy was applied to the HRTEM data of the heterogeneous combination $LiTmF_4/CaF_2$. The analysis of the FT patterns of different regions (Figure S12) confirms the inclusion of Tm into the

https://doi.org/10.1021/acsnano.4c07932
ACS Nano 2024, 18, 26233−26250

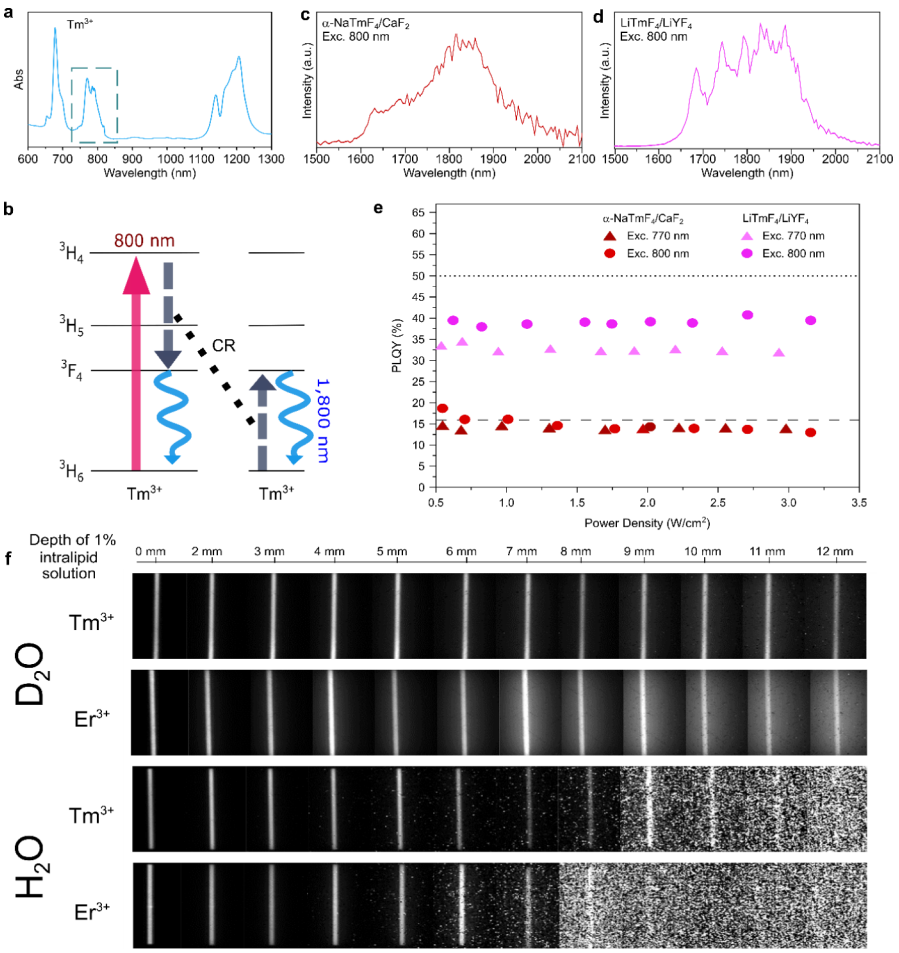

Figure 10. Tm^{3+}downshifting optical properties in the far-end of the SWIR region for homogeneous and heterogeneous material combinations. Typical absorption (abs) spectrum of Tm^{3+} ions with the dashed area representing the range of the used wavelengths for the excitation of Tm^{3+}-based homo- and heterostructured nanocrystals (a). Accepted downshifting mechanism for Tm^{3+} emission in the spectral region 1600−2100 nm involving cross-relaxation (CR) between Tm^{3+} atoms (b). Typical Tm^{3+} emission spectrum in the far-end of the SWIR region ($\lambda_{em.}$ 1600−2100 nm) for the heterogeneous α-$NaTmF_4/CaF_2$ (c) and homogeneous $LiTmF_4/LiYF_4$ (d) material combinations. Absolute power dependence downshifting photoluminescence quantum yield (PLQY) from 0.5 to 3.5 W/cm^2 for the heterogeneous α-$NaTmF_4/CaF_2$ (light- and dark-red symbols) and homogeneous $LiTmF_4/LiYF_4$ (light- and dark-pink symbols) material combinations (e). The dashed line represents the highest downshifting PLQY value for Tm^{3+} downshifting emission in the far-end of the SWIR region reported in the literature.[17] The dotted line represents the highest downshifting PLQY value for Er^{3+} downshifting emission in the 1400−1650 nm SWIR region reported by our group with a heterogeneous material combination.[32] Comparison of Er^{3+} and Tm^{3+} emission through different intralipid (1 vol % in either H_2O or D_2O) thicknesses (f). The incident power density was kept as close as possible to 50 mW/cm^2 for all images. Displayed intensity levels were optimized for each image.

crystal structure of the CaF_2 shell, which is in agreement with the results obtained by EDX and Rietveld refinement.

At this point, it is worth noting that the ability to discriminate between alloyed and core−shell structures (with or without intermixing) by PXRD or HRTEM (combined with FT) is highly dependent on the type of material combination. Indeed, the existence of unique features (e.g., zero-intensity of specific reflections) that are inherent to the diffraction patterns of the pure materials is an absolute prerequisite. For instance, in the case of the homogeneous material combination α-$NaTmF_4/NaYF_4$, neither PXRD nor HRTEM data (Figure S13) can be used to unambiguously discriminate between alloyed and core−shell structures (with or without intermixing). Indeed, the zero-intensity of specific reflections is no longer valid when CaF_2 is replaced by α-$NaYF_4$. Thus, only meticulous EM characterization based on EDX spectroscopy can be used to reveal the atomic scale organization. The same limitations apply to the homogeneous material combination $LiTmF_4/LiYF_4$ (Figure S14).

Effect of Material Combinations on Tm^{3+} SWIR Emission above 1600 nm. The downshifting SWIR emission properties of Tm^{3+} were assessed in the solid-state for all investigated material combinations. Figure 10a shows a typical absorption spectrum for Tm^{3+} in the NIR-SWIR region. Among all absorption bands, the one centered at 800 nm is often considered as the optimum excitation wavelength for bioimaging, as it overcomes the absorption peak of water in the range of 900−1050 nm (Figure S15). The widely accepted mechanism for Tm^{3+} emission above 1600 nm, illustrated in Figure 10b, involves cross-relaxation between the $^3H_4$ and $^3F_4$ electronic energy levels of two Tm^{3+} ions.[56] No luminescence was detected for the starting core NCs (α-$NaTmF_4$ and $LiTmF_4$), which was expected due to surface quenching. The latter is even exacerbated for small core NCs with a high concentration of optically active ions, as a multitude of energy

https://doi.org/10.1021/acsnano.4c07932
ACS Nano 2024, 18, 26233−26250

migration pathways to surface quenching sites are easily accessible. Interestingly, for the homogeneous (α-$NaTmF_4$/$NaYF_4$) and heterogeneous (α-$NaTmF_4$/$LiYF_4$) material combinations with the cubic core NCs (α-$NaTmF_4$), no emission was detected (Figure S16). Similarly, the Tm^{3+} emission was also not detectable for all heterogeneous material combinations ($LiTmF_4$/$NaYF_4$, $LiTmF_4$/CaF_2, Figure S17) with the tetragonal core NCs ($LiTmF_4$). The absence of Tm^{3+} emission for all these material combinations can be easily explained as the final homo- and heterostructured NCs exhibit complete (i.e., alloying) or partial (discrete doping) redistribution of Tm^{3+} throughout the entire volume of the particles without the existence of any pure protecting inert shell as initially anticipated. Therefore, the broken spatial confinement of the optically active centers (initially localized in the core domain) creates novel pathways for energy leakage to surface quenchers.

Out of the six investigated material combinations, only two exhibit Tm^{3+} emission above 1600 nm as illustrated by the broad emission bands observed for the heterogeneous cubic material combination (α-$NaTmF_4$/CaF_2 − Figures 10c and S18) and the homogeneous tetragonal material combination ($LiTmF_4$/$LiYF_4$ − Figures 10d and S19). The power-dependent absolute measurement of downshifting PLQYs was obtained at two different excitation wavelengths (770 and 800 nm, Figure 10e). For the cubic heterogeneous material combination (α-$NaTmF_4$/CaF_2), which forms a true core−shell structure with an abrupt interface, the downshifting PLQY is close to 14%. Note that such a PLQY value is very close to the highest PLQY values reported for Tm^{3+} emission above 1600 nm by Chang et al. (16%) and Yang et al. (14%).[17,57] It is also worth noting that the downshifting PLQY of the cubic heterogeneous material combination was boosted up to 24% (Figure S20) by lowering the quantity of Tm^{3+} in the starting core NCs down to 50% (α-$NaY_{0.5}Tm_{0.5}F_4$/CaF_2). As no chemical composition optimization was performed for the cubic heterogeneous material combination, the PLQY might still be improved for such a combination. Interestingly, the downshifting SWIR PLQY reaches a value of 39% (Figure 10e) for the tetragonal homogeneous material combination ($LiTmF_4$/$LiYF_4$), which forms a core−shell structure with a thick alloyed interphase in between the pure thin protecting shell ($LiYF_4$) and pure core ($LiTmF_4$) domains. Such a high PLQY value, to the best of our knowledge, has never been reported for SWIR emission in the far-end (>1600 nm) of the SWIR region and, although slightly weaker, is comparable to the highest PLQY value reported (49%) for Er^{3+} emission at 1550 nm (Figure 10e).[32]

Additionally, to measure the downshifting efficiency, fluorescence images were acquired to compare the potential of the most efficient material combination obtained ($LiTmF_4$/$LiYF_4$) with the performance of the previously reported heterogeneous material combination ($NaYF_4$:Yb:Er:Ce/CaF_2) for SWIR emission at ca. 1550 nm.[32] Fluorescence images were obtained at various depths within 1 vol % intralipid solutions, which are commonly used to represent light propagation in tissue, particularly the effect of photon scattering and absorbance.[58] To isolate these optical effects, intralipid solutions were prepared in both D_2O and H_2O. Indeed, in the SWIR spectral region of interest, the absorption of Tm^{3+} emission by H_2O is the dominating effect for a contrast decrease with penetration depth. On the other hand, in D_2O, the contrast decrease is mostly due to scattering (Figure S15). For the homogeneous material combination ($LiTmF_4$/$LiYF_4$), the scattering effect starts to be noticeable for thicknesses larger than 11 mm for downshifting Tm^{3+} emission ($\lambda_{ex.}$ = 785 nm) in the 1650−1950 nm range (Figure 10f − first row). On the contrary, for the heterogeneous material combination ($NaYF_4$:Yb:Er:Ce/CaF_2) for downshifting Er^{3+} emission ($\lambda_{ex.}$ = 968 nm) in the 1450−1650 nm range, scattering was observed at thicknesses as short as 4 mm (Figure 10f − second row). Intralipid solutions prepared in H_2O illustrate the advantage of the excitation wavelength at 800 nm compared to 980 nm. Indeed, even though the PLQY is larger in the case of the heterogeneous material combination ($NaYF_4$:Yb:Er:Ce/CaF_2) compared to the homogeneous material combination ($LiTmF_4$/$LiYF_4$), the Er^{3+} signal becomes undiscernible from the background for a penetration depth that is smaller compared to the one observed for the Tm^{3+} signal due to water absorption (Figure 10f − third and fourth rows). NIR-camera setup and extended figures related to the intralipid tests are available in the Supporting Information (Figures S21−S25).

DISCUSSION

Out of three material combinations with the exact same optically active cubic (α-$NaTmF_4$) core NCs, the Tm^{3+} emission above 1600 nm can only be observed for one combination (i.e., α-$NaTmF_4$/CaF_2). EDX chemical maps, EDX line scan analyses, and PXRD and HRTEM (when suitable) demonstrated that various material combinations with the same cubic core NCs and synthesized under the same experimental conditions lead to dramatically different chemical organizations with direct consequences on the SWIR emission performance of Tm^{3+}. Indeed, the magnitude of cation intermixing is totally modified depending on the type of shell material that is combined with the exact same starting cubic core NCs. For the homogeneous material combination between isostructural crystalline phases with the ability to easily form a solid solution (i.e., α-$NaTmF_4$ and α-$NaYF_4$), cation intermixing is severe and leads to full alloying, although nonhomogeneous. The same behavior is observed for the heterogeneous material combination involving different crystalline phases (α-$NaTmF_4$ and tetragonal $LiYF_4$). It is worth mentioning that despite the dissimilar crystal structures (cubic vs tetragonal), the selected tetragonal shell material did not nucleate separately as could have been expected. Not only the alloying option was preferred, but also the initial cubic crystal structure was nearly entirely converted to the tetragonal crystal structure. The energetically favored tetragonal crystal structure to the detriment of the cubic crystal structure acting as the driving force for the fragmentation and destruction of the starting core NCs can be ruled out, as the exact opposite was observed when growing a cubic shell on tetragonal core NCs ($LiTmF_4$/$NaYF_4$ combination). The heterogeneous material combination between isostructural crystalline phases with limited miscibility (i.e., α-$NaTmF_4$ and CaF_2) is the only one that succeeded in forming a true core−shell structure with no sign of cation intermixing between the core and shell domains in agreement with what our group recently reported.[32] It is important to emphasize that despite the fact that the lattice mismatch is very similar between the homogeneous (α-$NaTmF_4$/$NaYF_4$) and heterogeneous (α-$NaTmF_4$/CaF_2) material combinations involving isostructural materials, crystallographic considerations alone such as crystal structure matching and lattice mismatch are not sufficient to

https://doi.org/10.1021/acsnano.4c07932
ACS Nano 2024, 18, 26233−26250

predict *a priori* the magnitude of intermixing. Indeed, as the material combinations were synthesized under the same experimental conditions (solvent, capping agent, chemical precursors, shell precursor delivery, heating rate, aging time, and growth temperature), the interplay between crystallography and chemistry very likely plays a role. For instance, the shell precursors themselves might have an impact on the stability of the starting core NCs. Thus, the ease with which solid solutions between the core and shell materials can be formed might play an important role in determining the stability of the starting core NCs once in contact with the shell precursor(s).

The results obtained with the last three material combinations also demonstrate that it is currently impossible to predict the final chemical organization that can be obtained when simply considering the type of material combinations (homogeneous vs heterogeneous, isostructural vs nonisostructural, chemical miscibility of the different domains). Indeed, the exact same material combinations synthesized with the tetragonal ($LiTmF_4$) core NCs instead of the cubic (α-$NaTmF_4$) core NCs exhibit dramatic differences in two cases out of three.

Interestingly, heterogeneous combinations involving different crystal structures (i.e., tetragonal/cubic) lead to either the total destruction of the starting core NCs ($LiTmF_4/NaYF_4$) or the formation of a core−shell structure ($LiTmF_4/CaF_2$). As these combinations involve isostructural shell materials, it strengthens the hypothesis according to which the shell precursors modify the stability of the starting core NCs. Moreover, as the starting tetragonal phase is entirely destroyed when combined with α-$NaYF_4$, it is reasonable to assume that the solid-state miscibility of the core and shell materials is one of the driving forces. It is also important to note that although the heterogeneous $LiTmF_4/CaF_2$ material combination leads to the formation of a core−shell structure similar to the one formed with its isostructural counterpart (i.e., α-$NaTmF_4/CaF_2$), a major difference exists. Indeed, while in the latter case no Tm migrated in the CaF_2 shell, a small but constant concentration of Tm was detected in the former case, which was sufficient to fully quench the Tm SWIR emission. Interestingly, the homogeneous combination ($LiTmF_4/LiYF_4$) does not lead to full alloying but to the formation of a core−shell structure with an alloyed (nonhomogeneous) interphase in between the pure core and pure shell domains. The exceptionally high PLQY of 39% obtained for the homogeneous tetragonal material combination ($LiTmF_4/LiYF_4$) can be attributed to two important factors. First, the lower site symmetry of the tetragonal crystal structure ($\bar{4}$) compared to the highest site symmetry of the cubic crystal structure ($m\bar{3}m$) might be one important factor. It is indeed known that lower local symmetry relaxes Laporte's selection rules leading to facilitated 4f−4f transitions.[59,60] Second, the interphase observed in the homogeneous tetragonal material combination ($LiTmF_4/LiYF_4$) might play a role. Indeed, the best downshifting PLQY obtained for the only true core−shell structure (α-$NaTmF_4/CaF_2$) is not obtained for 100% Tm^{3+}, but for a significantly lower concentration (50% Tm^{3+} although not optimized). Therefore, the presence of a diffuse alloyed interphase might have played a role in optimizing interatomic distances between optically active centers. It is worth noting that despite investigating the same material combination as reported by Chang et al., the absolute downshifting PLQY of Tm^{3+} is significantly better (39% vs 14%).[17] This can be explained by considering the experimental conditions for the synthesis. Indeed, the precursors used for the syntheses reported in this article are water free (Figures S26−S30) while Chang et al. used heavily hydrated metal precursors in their synthesis protocol. Water in the reactive medium is a source of hydroxy groups that can be easily integrated into the crystal structure of ternary alkali metal RE-based fluorides. Haase et al. demonstrated the importance of maintaining an OH-free environment to obtain highly efficient upconversion.[61]

Finally, it is important to emphasize that out of the six investigated material combinations, Tm^{3+} SWIR downshifting luminescence can only be detected when a pure inert (i.e., no optically active element) shell is formed. The presence of Tm^{3+} in the outermost layer of the NCs with a high or low concentration is sufficient to fully quench the SWIR emission. This is due to the importance of protecting optically active core NCs from surface quenching sites as demonstrated two decades ago for RE-based luminescence (either downshifting or upconversion).[62,63] Later, the importance of blocking energy migration pathways to surface quenching sites has been demonstrated and used to tune and/or enhance the photoluminescence properties of RE-based NCs.[64−66] To date, the inert shell approach is still the most efficient strategy to optimize the performance of RE-based NCs. The results presented in this article are in agreement with known quenching mechanisms and demonstrate that although initially designed, the growth of a pure inert protecting shell is not guaranteed depending on the type of material combination.

CONCLUSIONS

Despite intensive research on RE-based core−shell NCs for more than two decades, the correlation between the atomic scale organization of an arbitrarily selected material combination (either homo- or heterostructured) and its PL properties has been poorly investigated. This article represents the first foray into investigating the consequences of various material combinations on the downshifting properties (Tm^{3+} SWIR emission above 1600 nm) of the synthesized homo- and heterostructured NCs.

The results reported in this article, obtained for a single set of experimental conditions with static characterizations of the final products, are highly enlightening to reveal the diversity behind the synthesis of RE-based core−shell NCs for which the "one-size-fits-all" model is definitely obsolete. It is important to emphasize that such diversity might even be exacerbated when changing one or several experimental parameters (e.g., growth temperature, nature of the shell precursor(s) etc.) with potentially different outcomes although dealing with the same material combination. The good news is that such diversity can be captured by the EDX spectroscopy toolbox (mapping and line scan analysis combined with the "subshell" approach). It is now established that for suitable material combinations such a toolbox can be wisely combined to PXRD and HRTEM (combined with FT) to extract accurate information regarding the atomic-scale organization of "core−shell" NCs. This can definitely help to pave the way toward the emergence of accurate atomistic 3D models of RE-based core−shell NCs.

This article demonstrates that the SWIR optical performance of Tm^{3+} above 1600 nm is well correlated to the true atomic-scale organization of the final NCs. Various material combinations, synthesized under the same experimental

https://doi.org/10.1021/acsnano.4c07932
ACS Nano 2024, 18, 26233−26250

conditions, can lead to drastically different atomic-scale organizations with consequences on the downshifting performance of Tm^{3+}. Indeed, depending on the type of material combination, the downshifting emission of Tm^{3+} in the far-end of the SWIR region spans a wide range from fully quenched (i.e., no emission) to highly efficient with a PLQY value of 39%. The latter is 2.4−2.8 times higher than the best PLQY values reported in the literature to date.

The experimental results of this article also demonstrate that the formation of true core−shell structures with RE-based NCs constitutes only one possibility among many others. It is important to emphasize that, out of six different material combinations investigated and synthesized under the same experimental conditions, only one (α-$NaTmF_4/CaF_2$) led to the formation of a true core−shell structure (i.e., core and shell domains perfectly segregated with an abrupt interface in between). Interestingly, the experimental results also revealed that the formation of a true core−shell structure with an abrupt interface does not seem to be a critical feature to maximize the optical performance, as long as a pure (i.e., without any trace of optically active atoms) protecting shell can be formed. Although the importance of the protecting outer shell to improve the PL performance of NCs in general and RE-based NCs in particular is not new, it is now demonstrated that the formation of such a protecting shell is absolutely not self-evident depending on the type of material combination. Thus, out of six different material combinations investigated and synthesized under the same experimental conditions, only two (α-$NaTmF_4/CaF_2$ and $LiTmF_4/LiYF_4$) end up with a pure protecting shell.

This article constitutes a significant step toward the emergence of informative guidelines to predict, in terms of atomic-scale organization, the outcome of a core−shell synthesis for various material combinations and experimental conditions. To increase the accuracy and prediction capabilities, this will ultimately require figuring out and rationalizing the underlying driving forces, molecular mechanisms, and dynamics involved in the formation of RE-based core−shell NCs under various experimental conditions. This article constitutes the first brick in the wall, and many others are required to reveal the big picture. Such a monumental piece of work, which is beyond the scope of this article, can be tackled only collectively. It is anticipated that the results of this article will significantly influence the field of RE-based NCs to optimize their optical performances by understanding (instead of assuming) their inherent structural and atomic scale organization under various experimental conditions. In the particular case of *in vivo* optical imaging in the far-end of the SWIR region, highly efficient NCs with emission in the 1650−1950 nm range can now be synthesized.

METHODS

Synthesis of α-$NaTmF_4$ Core NCs. Inside a glovebox under nitrogen, sodium trifluoroacetate (1 mmol), thulium trifluoroacetate (1 mmol), oleic acid (3.2 mL), oleylamine (3.3 mL), and octadecene (7.5 mL) were added to a 50 mL Schlenk flask. After dissolution of the starting trifluoroacetate precursors, the mixture was heated up (under argon) to 300 °C for 30 min. After cooling to room temperature, the core NCs were extracted, purified, and finally dispersed in chloroform. The resulting solution was stored in a glass vial under air. It was used as a stock solution for the subsequent growth of core−shell NCs with different material combinations. All experimental details regarding the synthesis of α-$NaTmF_4$ core NCs are given in the Supporting Information.

Synthesis of $LiTmF_4$ Core NCs. Inside a glovebox under nitrogen, lithium hydroxide (2.5 mmol) and ammonium fluoride (4 mmol) were added to a 10 mL glass vial together with 6 mL of methanol under constant stirring (ca. 90 min). In parallel, thulium trifluoroacetate (1 mmol), oleic acid (6 mL), and octadecene (15 mL) were added to a 50 mL Schlenk flask. After dissolution of the starting trifluoroacetate precursor, the methanol solution of lithium hydroxide and ammonium fluoride was injected (ca. 40 °C) into the 50 mL Schlenk flask. After aging at 70 °C for 30 min, methanol was removed under vacuum. The resulting mixture was heated up (under argon) to 300 °C for 60 min. After cooling down to room temperature, the core NCs were extracted, purified, and dispersed in chloroform. The resulting solution was stored in a glass vial under air. It was used as a stock solution for the subsequent growth of core−shell NCs with different material combinations. All experimental details regarding the synthesis of $LiTmF_4$ core NCs are given in the Supporting Information.

Synthesis of Core−Shell NCs. Inside a glovebox under nitrogen, 2 mmol of trifluoroacetate shell precursors was added to a 50 mL Schlenk flask together with oleic acid (7 mL) and ocatadecene (7 mL). Then, under an argon flow, 1 mL of stock solution of the starting core NCs (α-$NaTmF_4$ or $LiTmF_4$) was added to the 50 mL Schlenk flask. After dissolution of the starting trifluoroacetate precursors, the mixture was heated up (under argon) to 300 °C for 45 min. After cooling down to room temperature, the core−shell NCs were extracted, purified, and dispersed in chloroform. The resulting solution was stored in a glass vial and used for structural and optical characterizations. All experimental details regarding the synthesis of every material combination are given in the Supporting Information.

Structural Characterization of Core and Core−Shell NCs. PXRD patterns of core and core−shell NCs were acquired using a Bruker D8 Discover diffractometer with Bragg−Brentano geometry (CuKα1). The size, morphology, and chemical composition of core and core−shell NCs were investigated with FEI Osiris ChemiSTEM combined with a Super-X EDX detector. EDX line scans of individual NCs were obtained after quantifying the concentration profile of different chemical elements acquired along a line passing through the center of the corresponding NC. The EDX line scans were further analyzed by using the mathematical subshell approach based on various geometrical models for the shape of the core and shell domains. An aberration-corrected FEI Titan^3 operating at 300 kV was used for high-resolution imaging. Every structural characterization technique is described in detail in the Supporting Information.

Optical Characterization of Core and Core−Shell NCs. Absorption spectra were acquired with a PerkinElmer Lambda 950 UV/vis/IR spectrophotometer. Downshifting emission spectra and power-dependent PLQY were acquired with a homemade optical system. Absorption and emission measurements were performed by using two calibrated spectrometers (Zeiss, PGS NIR 2.2; Thorlabs, CCS200/M) to register the intensity of the sample emission and the excitation laser. The NCs were measured both in chloroform colloidal solution and in the solid state. All power-dependent PLQY measurements were repeated at least three times and averaged. All optical characterization techniques are described in detail in the Supporting Information.

https://doi.org/10.1021/acsnano.4c07932
ACS Nano 2024, 18, 26233−26250

SWIR Imaging. NCs were imaged using a custom setup equipped with an InGaAs camera and a specialized lens to prevent reflections. Filters were arranged to block off-angle laser reflections, and the NCs were excited using 785 and 968 nm lasers. The lasers were coupled to a fiber-optic bundle, passed through various optical components, and used to uniformly illuminate the sample. The power density was set to approximately 50 mW/cm^2. Images were captured at exposure times ranging from 0.25 to 30 ms, then processed for dark correction, averaging, and normalization. NC colloidal solutions were placed in capillary tubes for imaging, and intralipid solutions were used to achieve the desired thickness in a cell culture dish. All details regarding SWIR imaging are given in the Supporting Information.

ASSOCIATED CONTENT

Supporting Information

The Supporting Information is available free of charge at https://pubs.acs.org/doi/10.1021/acsnano.4c07932.

Experimental details regarding the synthesis of the starting metal precursors, core and core−shell NCs; surface functionalization of NCs for water transfer; PXRD, STEM, and HRTEM data acquisition; exact procedures for the acquisition of EDX chemical maps and line scans; detailed procedure for the measurement of absolute downshifting PLQY; SWIR imaging procedure of NCs in intralipid phantoms; details of all mathematical models used for the treatment of raw EDX line scans by the subshell approach (PDF)

AUTHOR INFORMATION

Corresponding Authors

Bryce S. Richards − *Karlsruhe Institute of Technology, Institute of Microstructure Technology, Eggenstein-Leopoldshafen 76344, Germany; Light Technology Institute, Karlsruhe Institute of Technology, Karlsruhe 76131, Germany;* orcid.org/0000-0001-5469-048X; Email: damien.hudry@kit.edu

Damien Hudry − *Karlsruhe Institute of Technology, Institute of Microstructure Technology, Eggenstein-Leopoldshafen 76344, Germany;* orcid.org/0000-0002-5167-7471; Email: bryce.richards@kit.edu

Authors

Fernando Arteaga Cardona − *Karlsruhe Institute of Technology, Institute of Microstructure Technology, Eggenstein-Leopoldshafen 76344, Germany*

Eduard Madirov − *Karlsruhe Institute of Technology, Institute of Microstructure Technology, Eggenstein-Leopoldshafen 76344, Germany*

Radian Popescu − *Karlsruhe Institute of Technology, Laboratory for Electron Microscopy, Karlsruhe 76131, Germany*

Di Wang − *Karlsruhe Institute of Technology, Institute of Nanotechnology and Karlsruhe Nano Micro Facility, Eggenstein-Leopoldshafen 76344, Germany;* orcid.org/0000-0001-9817-7047

Dmitry Busko − *Karlsruhe Institute of Technology, Institute of Microstructure Technology, Eggenstein-Leopoldshafen 76344, Germany*

Dominique Ectors − *Bruker AXS SE, Karlsruhe 76187, Germany*

Christian Kübel − *Karlsruhe Institute of Technology, Institute of Nanotechnology and Karlsruhe Nano Micro Facility, Eggenstein-Leopoldshafen 76344, Germany;* orcid.org/0000-0001-5701-4006

Yolita M. Eggeler − *Karlsruhe Institute of Technology, Laboratory for Electron Microscopy, Karlsruhe 76131, Germany*

Bernardo A. Arús − *Department of Functional Imaging in Surgical Oncology, National Center for Tumor Diseases (NCT/UCC), Dresden 01307, Germany; German Cancer Research Center (DKFZ), Heidelberg 69120, Germany; Medical Faculty and University Hospital Carl Gustav Carus, Dresden University of Technology (TUD), Dresden 01062, Germany; Helmholtz Zentrum Dresden-Rossendorf (HZDR), Dresden 01328, Germany; Helmholtz Pioneer Campus, Helmholtz Munich, Neuherberg 85764, Germany;* orcid.org/0000-0001-6132-7793

Andriy Chmyrov − *Department of Functional Imaging in Surgical Oncology, National Center for Tumor Diseases (NCT/UCC), Dresden 01307, Germany; German Cancer Research Center (DKFZ), Heidelberg 69120, Germany; Medical Faculty and University Hospital Carl Gustav Carus, Dresden University of Technology (TUD), Dresden 01062, Germany; Helmholtz Zentrum Dresden-Rossendorf (HZDR), Dresden 01328, Germany; Helmholtz Pioneer Campus, Helmholtz Munich, Neuherberg 85764, Germany*

Oliver T. Bruns − *Department of Functional Imaging in Surgical Oncology, National Center for Tumor Diseases (NCT/UCC), Dresden 01307, Germany; German Cancer Research Center (DKFZ), Heidelberg 69120, Germany; Medical Faculty and University Hospital Carl Gustav Carus, Dresden University of Technology (TUD), Dresden 01062, Germany; Helmholtz Zentrum Dresden-Rossendorf (HZDR), Dresden 01328, Germany; Helmholtz Pioneer Campus, Helmholtz Munich, Neuherberg 85764, Germany*

Complete contact information is available at: https://pubs.acs.org/10.1021/acsnano.4c07932

Notes

The authors declare no competing financial interest.

ACKNOWLEDGMENTS

This work was partly carried out with the support of the Karlsruhe Nano Micro Facility (KNMFi, www.knmf.kit.edu.), a Helmholtz Research Infrastructure at Karlsruhe Institute of Technology (KIT, www.kit.edu). The authors would like to acknowledge the financial support provided by the Helmholtz Association via: (i) the Professorial Recruitment Initiative Funding (B. Richards); (ii) the Research Field Energy − Program Materials and Technologies for the Energy Transition − Topic 1 Photovoltaics (F. Arteaga Cardona, D. Busko, E. Madirov, B. Richards, D. Hudry). O. Bruns and D. Hudry would like to thank the Helmholtz Imaging (ZT-I-PF-4-038-BENIGN). D. Hudry would like to thank the KIT Future Fields Initiative (HEALTH project).

REFERENCES

(1) Hudry, D.; Howard, I. A.; Popescu, R.; Gerthsen, D.; Richards, B. S. Structure−Property Relationships in Lanthanide-Doped Upconverting Nanocrystals: Recent Advances in Understanding Core−Shell Structures. *Adv. Mater.* **2019**, *31*, 1900623.

(2) Johnson, N. J. J.; van Veggel, F. C. J. M. Sodium Lanthanide Fluoride Core-Shell Nanocrystals: A General Perspective on Epitaxial Shell Growth. *Nano Res.* **2013**, *6*, 547−561.
(3) Hu, Q.; Kong, N.; Chai, Y.; Xing, Z.; Wu, Y.; Zhang, J.; Li, F.; Zhu, X. A Lanthanide Nanocomposite with Cross-Relaxation Enhanced near-Infrared Emissions as a Ratiometric Nanothermometer. *Nanoscale Horiz.* **2022**, *7*, 1177−1185.
(4) Yang, B.; Cang, J.; Li, Z.; Chen, J. Nanocrystals as Performance-Boosting Materials for Solar Cells. *Nanoscale Adv.* **2024**, *6*, 1331−1360.
(5) Zhang, C.; Yin, Q.; Ge, S.; Qi, J.; Han, Q.; Gao, W.; Wang, Y.; Zhang, M.; Dong, J. Optical Anti-Counterfeiting and Information Storage Based on Rare-Earth-Doped Luminescent Materials. *Mater. Res. Bull.* **2024**, *176*, 112801.
(6) Bruns, O. T.; Bischof, T. S.; Harris, D. K.; Franke, D.; Shi, Y.; Riedemann, L.; Bartelt, A.; Jaworski, F. B.; Carr, J. A.; Rowlands, C. J.; et al. Next-Generation in Vivo Optical Imaging with Short-Wave Infrared Quantum Dots. *Nat. Biomed. Eng.* **2017**, *1*, 0056.
(7) Zhao, M.; Sik, A.; Zhang, H.; Zhang, F. Tailored NIR-II Lanthanide Luminescent Nanocrystals for Improved Biomedical Application. *Adv. Opt. Mater.* **2023**, *11*, 2202039.
(8) He, S.; Song, J.; Qu, J.; Cheng, Z. Crucial Breakthrough of Second Near-Infrared Biological Window Fluorophores: Design and Synthesis toward Multimodal Imaging and Theranostics. *Chem. Soc. Rev.* **2018**, *47*, 4258−4278.
(9) Diao, S.; Blackburn, J. L.; Hong, G.; Antaris, A. L.; Chang, J.; Wu, J. Z.; Zhang, B.; Cheng, K.; Kuo, C. J.; Dai, H. Fluorescence Imaging In Vivo at Wavelengths beyond 1500 nm. *Angew. Chem., Int. Ed.* **2015**, *54*, 14758−14762.
(10) Iverson, N. M.; Barone, P. W.; Shandell, M.; Trudel, L. J.; Sen, S.; Sen, F.; Ivanov, V.; Atolia, E.; Farias, E.; McNicholas, T. P.; Reuel, N.; Parry, N. M. A.; Wogan, G. N.; Strano, M. S. In Vivo Biosensing via Tissue-Localizable near-Infrared-Fluorescent Single-Walled Carbon Nanotubes. *Nat. Nanotechnol.* **2013**, *8*, 873−880.
(11) Yomogida, Y.; Tanaka, T.; Zhang, M.; Yudasaka, M.; Wei, X.; Kataura, H. Industrial-Scale Separation of High-Purity Single-Chirality Single-Wall Carbon Nanotubes for Biological Imaging. *Nat. Commun.* **2016**, *7*, 12056.
(12) Gidwani, B.; Sahu, V.; Shukla, S. S.; Pandey, R.; Joshi, V.; Jain, V. K.; Vyas, A. Quantum Dots: Prospectives, Toxicity, Advances and Applications. *J. Drug Delivery Sci. Technol.* **2021**, *61*, 102308.
(13) Zhang, M.; Yue, J.; Cui, R.; Ma, Z.; Wan, H.; Wang, F.; Zhu, S.; Zhou, Y.; Kuang, Y.; Zhong, Y.; Pang, D.-W.; Dai, H. Bright Quantum Dots Emitting at ∼ 1,600 nm in the NIR-IIb Window for Deep Tissue Fluorescence Imaging. *Proc. Natl. Acad. Sci. U. S. A.* **2018**, *115*, 6590−6595.
(14) Wang, F.; Ren, F.; Ma, Z.; Qu, L.; Gourgues, R.; Xu, C.; Baghdasaryan, A.; Li, J.; Zadeh, I. E.; Los, J. W. N.; Fognini, A.; Qin-Dregely, J.; Dai, H. In Vivo Non-Invasive Confocal Fluorescence Imaging beyond 1,700nm Using Superconducting Nanowire Single-Photon Detectors. *Nat. Nanotechnol.* **2022**, *17*, 653−660.
(15) Hu, Z.; Fang, C.; Li, B.; Zhang, Z.; Cao, C.; Cai, M.; Su, S.; Sun, X.; Shi, X.; Li, C.; Zhou, T.; Zhang, Y.; Chi, C.; He, P.; Xia, X.; Chen, Y.; Gambhir, S. S.; Cheng, Z.; Tian, J. First-in-Human Liver-Tumour Surgery Guided by Multispectral Fluorescence Imaging in the Visible and near-Infrared-I/II Windows. *Nat. Biomed. Eng.* **2020**, *4*, 259−271.
(16) Hong, G.; Antaris, A. L.; Dai, H. Near-Infrared Fluorophores for Biomedical Imaging. *Nat. Biomed. Eng.* **2017**, *1*, 0010.
(17) Chang, Y.; Chen, H.; Xie, X.; Wan, Y.; Li, Q.; Wu, F.; Yang, R.; Wang, W.; Kong, X. Bright Tm^{3+}-Based Downshifting Luminescence Nanoprobe Operating around 1800nm for NIR-IIb and c Bioimaging. *Nat. Commun.* **2023**, *14*, 1079.
(18) Pitruzzello, G. Seeing into Deep Tissue. *Nat. Photonics* **2023**, *17*, 376−377.
(19) Feng, Z.; Tang, T.; Wu, T.; Yu, X.; Zhang, Y.; Wang, M.; Zheng, J.; Ying, Y.; Chen, S.; Zhou, J.; et al. Perfecting and Extending the Near-Infrared Imaging Window. *Light: Sci. Appl.* **2021**, *10*, 197.
(20) Chen, Z.-H.; Wang, X.; Yang, M.; Ming, J.; Yun, B.; Zhang, L.; Wang, X.; Yu, P.; Xu, J.; Zhang, H.; et al. An Extended NIR-II Superior Imaging Window from 1500 to 1900 nm for High-Resolution In Vivo Multiplexed Imaging Based on Lanthanide Nanocrystals. *Angew. Chem., Int. Ed.* **2023**, *62*, No. e202311883.
(21) Wang, X.; Valiev, R. R.; Ohulchanskyy, T. Y.; Ågren, H.; Yang, C.; Chen, G. Dye-Sensitized Lanthanide-Doped Upconversion Nanoparticles. *Chem. Soc. Rev.* **2017**, *46*, 4150−4167.
(22) Xu, H.; Dai, M.; Fu, Z. The Art of Nanoparticle Design: Unconventional Morphologies for Advancing Luminescent Technologies. *Small* **2024**, *20*, 2400218.
(23) Sheng, T.; Xu, M.; Li, Q.; Wu, Y.; Zhang, J.; Liu, J.; Zhu, X.; Zhang, Y. Elucidating the Role of Energy Management in Making Brighter, and More Colorful Upconversion Nanoparticles. *Mater. Today Phys.* **2021**, *20*, 100451.
(24) Zhang, Y.; Wen, R.; Hu, J.; Guan, D.; Qiu, X.; Zhang, Y.; Kohane, D. S.; Liu, Q. Enhancement of Single Upconversion Nanoparticle Imaging by Topologically Segregated Core-Shell Structure with Inward Energy Migration. *Nat. Commun.* **2022**, *13*, 5927.
(25) Huang, K.; Li, Z.; Li, Y.; Yu, N.; Gao, X.; Huang, L.; Lim, S. F.; Han, G. Three-Dimensional Colloidal Controlled Growth of Core−Shell Heterostructured Persistent Luminescence Nanocrystals. *Nano Lett.* **2021**, *21*, 4903−4910.
(26) Huang, F.; Bagheri, N.; Wang, L.; Ågren, H.; Zhang, J.; Pu, R.; Zhan, Q.; Jing, Y.; Xu, W.; Widengren, J.; Liu, H. Suppression of Cation Intermixing Highly Boosts the Performance of Core−Shell Lanthanide Upconversion Nanoparticles. *J. Am. Chem. Soc.* **2023**, *145*, 17621−17631.
(27) Li, F.; Tu, L.; Zhang, Y.; Huang, D.; Liu, X.; Zhang, X.; Du, J.; Fan, R.; Yang, C.; Krämer, K. W.; Marques-Hueso, J.; Chen, G. Size-Dependent Lanthanide Energy Transfer Amplifies Upconversion Luminescence Quantum Yields. *Nat. Photonics* **2024**, *18*, 440−449.
(28) Hudry, D.; Busko, D.; Popescu, R.; Gerthsen, D.; Abeykoon, A. M. M.; Kübel, C.; Bergfeldt, T.; Richards, B. S. Direct Evidence of Significant Cation Intermixing in Upconverting Core@Shell Nanocrystals: Toward a New Crystallochemical Model. *Chem. Mater.* **2017**, *29*, 9238−9246.
(29) Dühnen, S.; Haase, M. Study on the Intermixing of Core and Shell in $NaEuF_4$/$NaGdF_4$ Core/Shell Nanocrystals. *Chem. Mater.* **2015**, *27*, 8375−8386.
(30) Bastian, P. U.; Robel, N.; Schmidt, P.; Schrumpf, T.; Günter, C.; Roddatis, V.; Kumke, M. U. Resonance Energy Transfer to Track the Motion of Lanthanide Ions; What Drives the Intermixing in Core-Shell Upconverting Nanoparticles? *Biosensors* **2021**, *11*, 515.
(31) Shang, Z.; Ren, Y.; Nie, G.; Ma, X.; Gao, X. Deposited 2D/3D Perovskite Heterojunctions Though Vapor-Assisted Solution Process for Restraining Intermixing Between the Two Phases. *Trans. Electr. Electron. Mater.* **2024**, *25*, 187−193.
(32) Arteaga Cardona, F.; Jain, N.; Popescu, R.; Busko, D.; Madirov, E.; Arús, B. A.; Gerthsen, D.; De Backer, A.; Bals, S.; Bruns, O. T.; et al. Preventing Cation Intermixing Enables 50% Quantum Yield in Sub-15 nm Short-Wave Infrared-Emitting Rare-Earth Based Core-Shell Nanocrystals. *Nat. Commun.* **2023**, *14*, 4462.
(33) Wang, Y.-F.; Sun, L.-D.; Xiao, J.-W.; Feng, W.; Zhou, J.-C.; Shen, J.; Yan, C.-H. Rare-Earth Nanoparticles with Enhanced Upconversion Emission and Suppressed Rare-Earth-Ion Leakage. *Chem. - Eur. J.* **2012**, *18*, 5558−5564.
(34) Xie, Y.; Song, Y.; Sun, G.; Hu, P.; Bednarkiewicz, A.; Sun, L. Lanthanide-Doped Heterostructured Nanocomposites toward Advanced Optical Anti-Counterfeiting and Information Storage. *Light: Sci. Appl.* **2022**, *11*, 150.
(35) Zou, Q.; Marcelot, C.; Ratel-Ramond, N.; Yi, X.; Roblin, P.; Frenzel, F.; Resch-Genger, U.; Eftekhari, A.; Bouchet, A.; Coudret, C.; Verelst, M.; Chen, X.; Mauricot, R.; Roux, C. Heterogeneous Oxysulfide@Fluoride Core/Shell Nanocrystals for Upconversion-Based Nanothermometry. *ACS Nano* **2022**, *16*, 12107−12117.
(36) Ding, Y.; Gu, J.; Zhang, T.; Yin, A.-X.; Yang, L.; Zhang, Y.-W.; Yan, C.-H. Chemoaffinity-Mediated Synthesis of $NaRES_2$-Based

https://doi.org/10.1021/acsnano.4c07932
ACS Nano 2024, 18, 26233−26250

Nanocrystals as Versatile Nano-Building Blocks and Durable Nano-Pigments. *J. Am. Chem. Soc.* **2012**, *134*, 3255−3264.
(37) Wang, L.; Ren, L.; Mitchell, D.; Casillas-Garcia, G.; Ren, W.; Ma, C.; Xu, X. X.; Wen, S.; Wang, F.; Zhou, J.; Xu, X.; Hao, W.; Dou, S. X.; Du, Y. Enhanced Energy Transfer in Heterogeneous Nanocrystals for near Infrared Upconversion Photocurrent Generation. *Nanoscale* **2017**, *9*, 18661−18667.
(38) Dong, H.; Sun, L.-D.; Li, L.-D.; Si, R.; Liu, R.; Yan, C.-H. Selective Cation Exchange Enabled Growth of Lanthanide Core/Shell Nanoparticles with Dissimilar Structure. *J. Am. Chem. Soc.* **2017**, *139*, 18492−18495.
(39) Xu, F.; Gao, H.; Liang, J.; Jin, S.; Zhao, J.; Liu, Y.; Zhang, H.; Zhang, Z.; Mao, Y. Enhanced Upconversion Luminescence in $Cu_{1.8}S$@$NaYF_4$: Yb@ $NaYF_4$: Yb, Er Core-Shell Nanoparticles. *Ceram. Int.* **2019**, *45*, 21557−21563.
(40) de Sousa Ferreira, F.; de Morais, A. J.; Santos Calado, C. M.; Iikawa, F.; Couto Junior, O. D. D.; Brunet, G.; Murugesu, M.; Mazali, I. O.; Sigoli, F. A. Dual Magnetic Field and Temperature Optical Probes of Controlled Crystalline Phases in Lanthanide-Doped Multi-Shell Nanoparticles. *Nanoscale* **2021**, *13*, 14723−14733.
(41) Ruan, L.; Zhang, Y. NIR-Excitable Heterostructured Upconversion Perovskite Nanodots with Improved Stability. *Nat. Commun.* **2021**, *12*, 219.
(42) Xiao, H.; Liu, B.; Qiu, L.; Li, G.; Zhang, G.; Huang, D.; Zhao, Y.; Yang, C.; Jiang, F.; Dang, P.; et al. Core−Shell Structured Upconversion/Lead-Free Perovskite Nanoparticles for Anticounterfeiting Applications. *Angew. Chem., Int. Ed.* **2022**, *61*, No. e202115136.
(43) López-Peña, G.; Hamraoui, K.; Horchani-Naifer, K.; Gerke, C.; Ortgies, D. H.; Martín Rodríguez, E.; Chen, G.; Jaque, D.; Rubio Retama, J. Lanthanide Doped Nanoheaters with Reliable and Absolute Temperature Feedback. *Phys. B Condens. Matter* **2022**, *631*, 413652.
(44) Wu, R.; Zhou, J.; Lei, L.; Zhang, S.; Xiao, Z.; Zhang, J.; Xu, S. α-$NaYF_4$: Yb^{3+}-Tm^{3+}@CaF_2 Nanocrystals for NIR-to-NIR Temperature Sensing. *Chem. Phys. Lett.* **2017**, *667*, 206−210.
(45) Dong, H.; Sun, L.-D.; Wang, Y.-F.; Ke, J.; Si, R.; Xiao, J.-W.; Lyu, G.-M.; Shi, S.; Yan, C.-H. Efficient Tailoring of Upconversion Selectivity by Engineering Local Structure of Lanthanides in Na_xREF_{3+x} Nanocrystals. *J. Am. Chem. Soc.* **2015**, *137*, 6569−6576.
(46) Shen, J.; Chen, G.; Ohulchanskyy, T. Y.; Kesseli, S. J.; Buchholz, S.; Li, Z.; Prasad, P. N.; Han, G. Tunable Near Infrared to Ultraviolet Upconversion Luminescence Enhancement in (α-$NaYF_4$: Yb,Tm)/CaF_2 Core/Shell Nanoparticles for In Situ Real-Time Recorded Biocompatible Photoactivation. *Small* **2013**, *9*, 3213−3217.
(47) Chen, G.; Shen, J.; Ohulchanskyy, T. Y.; Patel, N. J.; Kutikov, A.; Li, Z.; Song, J.; Pandey, R. K.; Ågren, H.; Prasad, P. N.; Han, G. (α-$NaYbF_4$: Tm^{3+})/CaF_2 Core/Shell Nanoparticles with Efficient Near-Infrared to Near-Infrared Upconversion for High-Contrast Deep Tissue Bioimaging. *ACS Nano* **2012**, *6*, 8280−8287.
(48) Hudry, D.; De Backer, A.; Popescu, R.; Busko, D.; Howard, I. A.; Bals, S.; Zhang, Y.; Pedrazo-Tardajos, A.; Van Aert, S.; Gerthsen, D. Interface Pattern Engineering in Core-Shell Upconverting Nanocrystals: Shedding Light on Critical Parameters and Consequences for the Photoluminescence Properties. *Small* **2021**, *17*, 2104441.
(49) Shannon, R. D. Revised Effective Ionic Radii and Systematic Studies of Interatomic Distances in Halides and Chalcogenides. *Acta Crystallogr.* **1976**, *32*, 751−767.
(50) Scardi, P. Diffraction Line Profiles in the Rietveld Method. *Cryst. Growth Des.* **2020**, *20*, 6903−6916.
(51) Scardi, P.; Azanza Ricardo, C. L.; Perez-Demydenko, C.; Coelho, A. A. Whole Powder Pattern Modelling Macros for TOPAS. *J. Appl. Crystallogr.* **2018**, *51*, 1752−1765.
(52) Kind, C.; Popescu, R.; Schneider, R.; Müller, E.; Gerthsen, D.; Feldmann, C. Advanced Bimetallic In−Cu/Ag/Au Nanostructures via Microemulsion-Based Reaction. *RSC Adv.* **2012**, *2*, 9473−9487.
(53) Ectors, D.; Goetz-Neunhoeffer, F.; Neubauer, J. A Generalized Geometric Approach to Anisotropic Peak Broadening Due to Domain Morphology. *J. Appl. Crystallogr.* **2015**, *48*, 189−194.
(54) *Debyer*. https://debyer.readthedocs.io/en/latest/#direct-space-patterns. Visited in March 2024.
(55) Gelisio, L.; Scardi, P. 100 Years of Debye's Scattering Equation. *Acta Crystallogr.* **2016**, *72*, 608−620.
(56) Ganem, J.; Crawford, J.; Schmidt, P.; Jenkins, N. W.; Bowman, S. R. Thulium Cross-Relaxation in a Low Phonon Energy Crystalline Host. *Phys. Rev. B* **2002**, *66*, 245101.
(57) Yang, Y.; Chen, Y.; Pei, P.; Fan, Y.; Wang, S.; Zhang, H.; Zhao, D.; Qian, B.-Z.; Zhang, F. Fluorescence-Amplified Nanocrystals in the Second near-Infrared Window for in Vivo Real-Time Dynamic Multiplexed Imaging. *Nat. Nanotechnol.* **2023**, *18*, 1195−1204.
(58) Wang, F.; Zhong, Y.; Bruns, O.; Liang, Y.; Dai, H. In Vivo NIR-II Fluorescence Imaging for Biology and Medicine. *Nat. Photonics* **2024**, *18*, 535−547.
(59) Wisser, M. D.; Chea, M.; Lin, Y.; Wu, D. M.; Mao, W. L.; Salleo, A.; Dionne, J. A. Strain-Induced Modification of Optical Selection Rules in Lanthanide-Based Upconverting Nanoparticles. *Nano Lett.* **2015**, *15*, 1891−1897.
(60) Liang, L.; Feng, Z.; Zhang, Q.; Cong, T. D.; Wang, Y.; Qin, X.; Yi, Z.; Ang, M. J. Y.; Zhou, L.; Feng, H.; Xing, B.; Gu, M.; Li, X.; Liu, X. Continuous-Wave near-Infrared Stimulated-Emission Depletion Microscopy Using Downshifting Lanthanide Nanoparticles. *Nat. Nanotechnol.* **2021**, *16*, 975−980.
(61) Würth, C.; Grauel, B.; Pons, M.; Frenzel, F.; Rissiek, P.; Rücker, K.; Haase, M.; Resch-Genger, U. Yb- and Er Concentration Dependence of the Upconversion Luminescence of Highly Doped $NaYF_4$: Yb,Er/$NaYF_4$: Lu Core/Shell Nanocrystals Prepared by a Water-Free Synthesis. *Nano Res.* **2022**, *15*, 9639−9646.
(62) Yi, G.-S.; Chow, G.-M. Water-Soluble $NaYF_4$: Yb,Er(Tm)/$NaYF_4$/Polymer Core/Shell/Shell Nanoparticles with Significant Enhancement of Upconversion Fluorescence. *Chem. Mater.* **2007**, *19*, 341−343.
(63) Kömpe, K.; Borchert, H.; Storz, J.; Lobo, A.; Adam, S.; Möller, T.; Haase, M. Green-Emitting $CePO_4$: Tb/$LaPO_4$ Core−Shell Nanoparticles with 70%Photoluminescence Quantum Yield. *Angew. Chem., Int. Ed.* **2003**, *42*, 5513−5516.
(64) Su, Q.; Han, S.; Xie, X.; Zhu, H.; Chen, H.; Chen, C.-K.; Liu, R.-S.; Chen, X.; Wang, F.; Liu, X. The Effect of Surface Coating on Energy Migration-Mediated Upconversion. *J. Am. Chem. Soc.* **2012**, *134*, 20849−20857.
(65) Wang, F.; Deng, R.; Wang, J.; Wang, Q.; Han, Y.; Zhu, H.; Chen, X.; Liu, X. Tuning Upconversion through Energy Migration in Core−Shell Nanoparticles. *Nat. Mater.* **2011**, *10*, 968−973.
(66) Wang, F.; Wang, J.; Liu, X. Direct Evidence of a Surface Quenching Effect on Size-Dependent Luminescence of Upconversion Nanoparticles. *Angew. Chem., Int. Ed.* **2010**, *49*, 7456−7460.

https://doi.org/10.1021/acsnano.4c07932
ACS Nano 2024, 18, 26233−26250